Fatty acid amide hydrolase inhibition for treatment of amyotrophic lateral sclerosis

Authors: Daisuke Ito [1,2]*, Madoka Iida[1], Yohei Iguchi[1], Atsushi Hashizume[2], Shinichiro Yamada[1], Yoshiyuki Kishimoto[1], Shota Komori[1], Kazuki Obara[1], Shuto Nishisaki[3], Satoshi Yokoi[1,3], Teppei Shimamura[4], Yuto Takemoto[5], Masahiro Nakatochi[5], Tomohiro Akashi[4], Kunihiko Hinohara[6,7], Hyeon-Cheol Lee-Okada[8], Yohei Okada[9], Junichi Niwa[10], Gen Sobue[11], Shinji Tanaka[12], Ken Takashina[12], Takehiko Yokomizo[8], Masahisa Katsuno[1]*

Author affiliations:

[1]Department of Neurology, Nagoya University Graduate School of Medicine; Nagoya, Aichi, Japan.

[2]Department of Clinical Research Education, Nagoya University Graduate School of Medicine; Nagoya, Aichi, Japan.

[3]Department of Pathophysiological Laboratory Sciences, Nagoya University Graduate School of Medicine; Nagoya, Aichi, Japan.

[4]Division of Systems Biology, Nagoya University Graduate School of Medicine; Nagoya, Aichi, Japan.

[5]Public Health Informatics Unit, Department of Integrated Health Sciences, Nagoya University Graduate School of Medicine; Nagoya, Aichi, Japan.

[6]Department of Immunology, Nagoya University Graduate School of Medicine; Nagoya, Aichi, Japan.

[7]Institute for Advanced Research, Nagoya University; Nagoya, Aichi, 464-8601, Japan.

[8]Department of Biochemistry, Juntendo University Graduate School of Medicine; Bunkyo-ku, Tokyo, Japan.

[9]Department of Neural iPSC Research Institute for Medical Science of Aging, Aichi Medical University; Nagakute, Aichi, Japan.

[10]Department of Neurology, Aichi Medical University School of Medicine; Nagakute, Aichi, Japan.

[11]Aichi Medical University School of Medicine; Nagakute, Aichi, Japan.

[12]Sohyaku, Innovative Research Division, Mitsubishi Tanabe Pharma Corporation; Yokohama, Japan.

*Correspondence to: Masahisa Katsuno, or Daisuke Ito

Masahisa Katsuno, MD, PhD

Department of Neurology, Nagoya University Graduate School of Medicine

65 Tsurumai-cho, Showa-ku, Nagoya 466-8550 Japan

TEL: +81-52-744-2389; FAX: +81-52-744-2384

E-mail: katsuno.masahisa.i1@f.mail.nagoya-u.ac.jp

Daisuke Ito, MD, PhD.

Department of Neurology, Nagoya University Graduate School of Medicine

65 Tsurumai-cho, Showa-ku, Nagoya 466-8550 Japan

TEL: +81-52-744-2390; FAX: +81-52-744-2394

E-mail: ito.daisuke.k4@f.mail.nagoya-u.ac.jp

Competing Interests

This study was partially supported by Mitsubishi-Tanabe Pharma. ST and KT are employees of Mitsubishi-Tanabe Pharma. Nagoya University has filed a patent related to this manuscript: PCT application PCT/JP2022/018823, entitled “PROPHYLACTIC AND/OR THERAPEUTIC AGENT FOR AMYOTROPHIC LATERAL SCLEROSIS” with DI, YI, and MK as coinventor.

Abstract (<200 words)

Amyotrophic lateral sclerosis (ALS) is a devastating neurodegenerative disease caused by the selective loss of upper and lower motor neurons. There is a considerable variability in the disease progression of sporadic ALS, but the molecular basis for phenotypic heterogeneity remains largely unknown. ALS patients often manifest systemic metabolic abnormalities such as glucose intolerance and hypermetabolic state. We conducted reverse translational research to explore therapeutic targets in ALS based on the systemic metabolic alterations in patients and identified several metabolites associated with the disease progression, including metabolites involved in the expanded endocannabinoid system (ECS). In particular, the levels of *N*-acyl taurines (NATs) were correlated with the longitudinal change in the revised ALS functional rating scale and survival. Experiments with ALS cellular models, iPS cells derived from ALS patients and $SOD1^{G93A}$ transgenic mice revealed that PF-04457845, a fatty acid amide hydrolase inhibitor, upregulated the expanded ECS, particularly the levels of NATs and ameliorated motor neuron degeneration through the regulation of microglial environment, synapse plasticity, and neuronal development. These results collectively indicate that dysregulation of NATs is associated with ALS progression and PF-04457845 may represent a potential disease-modifying therapy for ALS.

(188 words)

Keywords: amyotrophic lateral sclerosis; *N*-acyl taurine; expanded endocannabinoid system; fatty acid amide hydrolase inhibitor; metabolomics.

Background

Amyotrophic lateral sclerosis (ALS) is a devastating neurodegenerative disease caused by the selective loss of upper and lower motor neurons. Approximately 95% of ALS cases are sporadic, and 5% are familial. Causative genes for familial ALS are diverse, including *superoxide dismutase 1* (*SOD1*), *TARDBP*, and *C9ORF72* (1–7). A *SOD1*-based murine model has been widely used for the preclinical study of ALS therapeutic strategies because it simulates the rapid progression of motor neuron degeneration and glial cell changes characteristic of human ALS pathology. In sporadic ALS, muscle weakness and atrophy rapidly progress, and the time from onset to death is around 3–5 years, mainly as a result of respiratory failure (8, 9). However, it is widely known that there is a considerable variability in the disease progression of sporadic ALS. This variability suggests that biological factors governing disease progression may be a therapeutic target of sporadic ALS, but the molecular basis for ALS phenotypic heterogeneity remains elusive.

A great number of therapeutics for ALS that showed efficacy in preclinical studies failed in clinical trials (10, 11). Although riluzole and edaravone have been approved for ALS treatment, their efficacies are limited (12, 13). These difficulties in therapy development are, at least partially, due to the discrepancy between the molecular changes in human sporadic ALS and those in cell or animal models established by implementing familial ALS gene mutations; the cell and animal models expressing the causative gene mutations of familial ALS do not necessarily reflect the pathological mechanism of human sporadic ALS. Therefore, the development of therapeutics should be based on human ALS pathophysiology. An approach to overcome these struggles is the utilization of induced pluripotent stem (iPS) cells derived from human ALS patients (14). Indeed, drug screening using motor neurons differentiated from iPS cells identified several candidates for ALS therapeutics (15, 16).

However, this approach alone is insufficient to target glial pathology, which plays fundamental roles in ALS progression (17–20). Thus, more comprehensive approaches are needed to achieve reverse translational therapy development based on human ALS pathophysiology.

Patients with sporadic ALS often develop a pathological condition called hypermetabolism, a severe weight loss due to excess resting energy expenditure, which is related to rapid progression and poor prognosis of ALS (21–23). In addition, glucose intolerance and dyslipidemia have also been reported in ALS patients, even at a prodromal stage of disease (24, 25). Nutritional intervention with a high-calorie and/or high-fat diet suppresses disease progression in certain populations of sporadic ALS patients (26, 27). These observations suggest a causative role of systemic metabolic changes in ALS.

Herein, we aimed to develop a therapeutic strategy for ALS with a special focus on metabolic alterations in patients by reverse translating clinical observations to basic research. We first conducted a clinical study to elucidate metabolic changes related to disease progression, screened compounds targeting the identified metabolic profiles in cellular models, and then tested a hit compound, a fatty acid amide hydrolase inhibitor, PF-04457845 in motor neurons differentiated from iPS cells (iPS-MN) derived from ALS patients and a mouse model of ALS. Our study identified that the dysregulation of *N*-acyl taurines (NATs), endogenous lipid mediators belonging to the expanded endocannabinoid system (ECS), is associated with disease progression in patients with sporadic ALS and that a pharmacological approach that activates NATs and the expanded ECS is a potential therapeutic strategy for ALS.

Results

Serum metabolome and lipid mediator analysis in sporadic ALS patients

The serum metabolome was analyzed in subjects with sporadic ALS and healthy controls. A total of 26 subjects with ALS and 10 healthy controls were analyzed in the discovery cohort (Figure 1A). The median longitudinal change in the revised ALS Functional Rating Scale (ALSFRS-R) at 6 months (slope ALSFRS-R) was -0.67/month (equivalent to 4-point decline over 6 months). Therefore, subjects with ALS whose decline of ALSFRS-R for 6 months was more than 5 points were defined as having rapidly progressive ALS (Rapid ALS, n = 12), and the others were defined as having slowly progressive ALS (Slow ALS, n = 14). Baseline characteristics were not different between the subjects in the Rapid ALS and Slow ALS groups (Supplemental Table S1 and S2). The Kaplan-Meier curve with the primary endpoint of the introduction of tracheostomy positive pressure ventilation (TPPV) or death clearly separated Rapid ALS and Slow ALS (Figure 1B). These findings confirmed the validity of the criteria used for categorizing ALS patients based on the longitudinal changes in ALSFRS-R scores. Sera of ALS patients and healthy controls were subjected to metabolome analysis using Metabolon UPLC-MS/MS.

Serum metabolomics detected 867 metabolites in total. Thirteen metabolites were significantly different among the three groups: Rapid ALS, Slow ALS and healthy controls (Supplemental Figure S1 and Supplemental Table S3). Random forest analysis, whose predictive accuracy for discrimination of three groups was 61%, which is above random chance, showed that *N*-linoleoyl taurine, a metabolite belonging to *N*-acyl taurine (NAT), was the most effective metabolite for distinguishing the groups (Figure 1C). *N*-acyl taurines (NATs) are taurine molecules conjugated to fatty acyl chains, and *N*-linoleoyl taurine is one representative species within this class. The top-ranked metabolites in the random forest analysis were mainly related to the expanded ECS including NATs, nucleic sugar, acylcarnitine, and polyamine metabolism. Similarly, sparse partial least squares discriminant

147 analysis (sPLS-DA) and heatmap analysis also demonstrated that NATs, nucleic sugar,
148 acylcarnitine, and polyamine metabolites were the discriminant metabolic factors for the
149 three groups (Figure 1, D–F).

150 To identify metabolic factors relevant to the disease progression of ALS, we further
151 performed a comparison between the Rapid ALS and Slow ALS groups. Volcano plot and
152 heatmap analyses showed an increase in NATs and polyamine metabolites in the Rapid ALS
153 group, and pathway enrichment analyses also showed alterations in those metabolic pathways
154 (Figure 2A, Supplemental Figures S2–S4). In addition, altered levels of bile acid metabolites
155 were also found in the Rapid ALS group with pathway analyses (Supplemental Figure S3 and
156 Supplemental Table S4). According to these clinical metabolome analyses, we selected five
157 metabolic pathways, NATs, polyamine/arginine, xanthine, bile acid, and acylcarnitine
158 metabolism, as candidate metabolic biomarkers associated with the progression of ALS.
159 Detailed alterations in identified metabolic pathways among the three groups are presented in
160 Supplemental Table S5.

161 Among the identified metabolic pathways, the alterations of NATs were prominent,
162 which belong to the expanded endocannabinoid system and act as a lipid mediators. To
163 validate the changes in *N*-acyl taurines, we performed a comprehensive lipid mediator
164 analysis in the replication cohort (ALS, n = 55; healthy controls, n = 25) (Figure 1A). The
165 smaller number of analytes detected in the replication cohort likely resulted from the use of a
166 targeted lipid mediator validation assay, in contrast to the broad untargeted metabolomics
167 platform used for the discovery cohort. Among the 75 lipid mediators analyzed, *N*-acyl
168 taurine levels were higher in the Rapid ALS group compared to the Slow ALS group,
169 consistent with the discovery cohort, demonstrating reproducible results (Figure 2, A and B).
170 A detailed analysis of the four detected *N*-acyl taurine species revealed that, in both cohorts,
171 their concentrations were elevated in the Rapid ALS group compared to healthy controls and

the Slow ALS group. Furthermore, their levels showed a correlation with the rate of disease progression, as indicated by the slope of ALSFRS-R (Figure 2, C–R). When analyzed separately by sex, similar trends were observed in both male and female patients in both cohorts (Supplemental Figures S5 and S6). In addition, survival analyses were conducted by stratifying patients in both cohorts into two groups based on the median serum concentrations of each NAT. These analyses revealed that patients with higher NAT levels exhibited shorter survival durations, and this trend was consistently observed across both cohorts (Figure 3). These findings are also consistent with the observed correlations between NAT levels and disease progression rates. The other metabolites in the ECS such as *N*-acyl ethanolamines (NAE) were not altered among the three groups (Supplemental Figure S7).

In vitro drug screening

The results of the clinical study on the relationship between the metabolome and disease progression of sporadic ALS patients led us to drug screening using cellular models of ALS. A total of 29 chemical compounds that potentially modulate the focused metabolic pathways (the expanded ECS including NATs, polyamine/arginine, xanthine, bile acid, and acylcarnitine), together with riluzole and edaravone as controls, were administered to two cellular models of ALS: NSC-34 cells transiently expressing mutant TDP-43^{A315T} and those expressing mutant SOD1^{G93A} (Figure 4 and Supplemental Table S6). The 29 compounds were selected as a representative and experimentally feasible set of modulators for the progression-related metabolic pathways identified in the patient metabolomics data, with emphasis on translational relevance and suitability for human use whenever possible. Cell viability was assessed using a water-soluble tetrazolium (WST) assay. Among the tested compounds, intervention in the endocannabinoid system demonstrated the most pronounced effect. PF-04457845 and *N*-stearoyl taurine improved cell viability in both models in a concentration-dependent manner (Figure 4, B and D). Additionally, *N*-palmitoyl taurine improved cell

viability in both models, although efficacy was observed at a single concentration (Figure 4E). While arachidonoyl ethanolamide (AEA, anandamide) improved the viability of NSC-34 cells expressing mutant TDP-43^{A315T}, such efficacy was not verified in the cells expressing mutant SOD1^{G93A} (Figure 4C). The efficacies of PF-04457845 and *N*-stearoyl taurine were further investigated by assessing lactate dehydrogenase (LDH) release. The results demonstrated a significant reduction in LDH release (Figure 4, F and G), corroborating their potential as therapeutic agents. To evaluate its effect in a human ALS disease model, we further administered PF-04457845 to motor neurons differentiated from iPS cells (iPS-MN) derived from three ALS patients (Figure 4H). Concentration-dependent neuroprotective effects were demonstrated by IncuCyte SX5® (Figure 4, I–L) and LDH assay (Figure 4M), as evidenced by preserved neurite length, number of cell clusters, and reduced LDH release. No significant line-dependent difference in treatment effect was detected among the iPSC lines. To assess disease specificity in vitro, PF-04457845 was also evaluated in mock-transfected NSC-34 cells and control iPSC-derived motor neurons; however, no significant effect of treatment was observed on WST-8 assay or LDH release in mock-transfected NSC-34 cells, or on neuronal morphology or LDH release in control iPSC-derived motor neurons (Supplemental Figure S8 and S9). These data suggest that PF-04457845 has potential as a therapeutic candidate for ALS.

PF-04457845 is a fatty acid amide hydrolase (FAAH) inhibitor. FAAH degrades NATs and NAEs, and knockdown of FAAH partially attenuates motor dysfunction in SOD1^{G93A} transgenic mice (28). Based on the results of cellular screening and the putative mechanism of the hit compounds, we further investigated PF-04457845 in vivo.

In vivo analysis of hit compounds in SOD1^{G93A} transgenic mice

The treatment of SOD1^{G93A} transgenic mice with PF-04457845 was started at the age of 8 weeks and continued until the ethical endpoint. Body weight measurements, grip strength and

rotarod tests were repeated weekly from the age of 8 weeks to 19 weeks, which was the end stage of this model. PF-04457845 was mixed with chow at a dose of 0.001%, which corresponded to ~1 mg/kg/day, and was administered to $SOD1^{G93A}$ transgenic mice. The survival of $SOD1^{G93A}$ transgenic mice administered PF-04457845 was extended by 8.5 days compared with that of untreated mice (Figure 5A). The administration of PF-04457845 significantly improved grip strength and rotarod test, whereas body weight was not significantly different (Figure 5, B–D). Survival and motor functional tests were also analyzed separately by the sex of the mice, yielding similar results (male mice, Supplemental Figure S10, A–D; female mice, Supplemental Figure S10, E–H). To assess possible nonspecific effects, PF-04457845 was also administered to wild-type C57BL/6 and B6/SJL mice. However, no significant effect of treatment was observed on body weight, grip strength, or rotarod performance, supporting the idea that its beneficial effects are disease-specific (Supplemental Figures S11 and S12).

To examine the effect of PF-04457845 on the motor neurons of $SOD1^{G93A}$ transgenic mice, paraffin-embedded sections of lumbar spinal cord (L5) samples from 16-week-old mice were analyzed by immunohistochemistry. The number of motor neurons with immunoreactivity for choline acetyltransferase within the lumbar spinal cord was significantly preserved in the $SOD1^{G93A}$ mice treated with PF-04457845 compared with untreated mice (Figure 5, E and F). The proliferation of astrocytes, microglia and oligodendrocytes was evaluated with anti-glial fibrillary acidic protein (GFAP) antibody (Figure 5, G and H), anti-ionized calcium-binding adapter molecule 1 (IBA-1) antibody (Figure 5, I and J), and anti Sry-related HMG-BOX gene 10 (SOX10) antibody (Figure 5, K and L), respectively. The proportion of astrocytes was significantly decreased by PF-04457845 treatment, although the proportions of microglia and oligodendrocytes were unchanged.

Lipidomics analysis of the murine spinal cords

To clarify the influence of PF-04457845 on lipid metabolism, a comprehensive lipidomics analysis was conducted on the spinal cords of three distinct groups: wild-type mice, untreated SOD1^{G93A} transgenic mice, and SOD1^{G93A} transgenic mice treated with PF-04457845. A total of 799 lipid metabolites were identified in the process (Supplemental Table S7). Subsequent sPLS-DA analysis effectively segregated these three groups, underscoring that the differentiation was primarily attributed to the concentrations of NATs and NAEs, both of which are known substrates of FAAH (Figure 6, A and B). By examining the levels of specific metabolites belonging to NATs and NAEs, we found that both lipids experienced an increase after treatment with PF-04457845, demonstrating that orally administered PF-04457845 successfully upregulates NATs and NAEs in the central nervous system of the SOD1^{G93A} transgenic mice. (Figure 6, C and D). Furthermore, three of the four NAT species identified in the sera of ALS patients—*N*-palmitoyl taurine(16:0), *N*-stearoyl taurine(18:0), and *N*-oleoyl taurine(18:1)—were detected by lipidomics. Notably, the levels of all these NATs were elevated in the spinal cord of untreated SOD1^{G93A} transgenic mice compared to wild-type mice, being consistent with the increase observed in Rapid ALS patients. Such changes were not observed for NAEs (Figure 6, C–E, Supplemental Figure S13). These results indicate that elevation of neural NATs levels represents a common pathogenic mechanism shared by SOD1^{G93A} transgenic mice and patients with Rapid ALS.

RNA and protein analysis of the spinal cord of SOD1^{G93A} transgenic mice treated with PF-04457845

To explore the mechanism of phenotypic amelioration in SOD1^{G93A} transgenic mice by PF-04457845, we performed RNA-Seq on their spinal cord. Enrichment analysis of the RNA-

Seq data revealed significant involvement of pathways related to macrophage and microglial differentiation and lipoprotein metabolism in PF-04457845-treated mice (n = 4) compared with untreated mice (n = 4) (Figure 7, A and B, Supplemental Table S8) Ingenuity Pathway Analysis (IPA) of the RNA-Seq data revealed activation of the interleukin-13 (IL-13) pathway in $SOD1^{G93A}$ transgenic mice treated with PF-04457845 (Figure 7C). In line with this finding, *Cd36*, a downstream molecule of IL-13, was up-regulated in the spinal cord of PF-04457845-treated mice (Supplemental Figure S14). $CD36^{+}$ microglia regulate lipid metabolism, promote myelin debris clearance, and support antioxidant responses (29, 30). Lipoprotein lipase (LPL) is also known to be expressed in microglial subtypes such as disease-associated microglia (DAM) and proliferative-region-associated microglia (PAM)(31, 32). Stimulation of CB2, an endocannabinoid receptor expressed on microglia, is reported to suppress inflammatory signaling and promote an anti-inflammatory, metabolically supportive microglial state (33, 34). Therefore, we examined microglial markers and molecules downstream of CB2 receptor signaling in the mouse spinal cord by Western blotting. ERK1/2 are key kinases in the MAPK pathway and function as downstream effectors of cannabinoid receptor associated signaling. The ratio of phosphorylated ERK1/2 to total ERK1/2 was increased in PF-04457845-treated mice compared with untreated mice, suggesting activation of the CB1/CB2 signaling pathway (Figure 7, D and E) (35). The protein levels of IBA-1 were not significantly changed by PF-04457845 treatment, consistent with the histopathological findings (Figure 7, D and F). The protein levels of CD86, a pro-inflammatory microglial marker, were decreased whereas those of CD36 and LPL were increased in PF-04457845-treated mice, supporting a shift toward a neuroprotective microglial phenotype (Figure 7, D, G–I). The expression of SOD1 was not affected by PF-04457845 (Figure 7, D and J).

Transcriptome alteration in neurons by PF-04457845

The bulk RNA-Seq of the spinal cord primarily revealed altered signaling related to the CB2 receptor, which is mainly expressed in microglia and oligodendrocytes. Given that neurons, as well as astrocytes, express CB1 receptors, the treatment-related changes in neurons did not appear to be reflected in the RNA-Seq data. To examine the impacts of treatment with PF-04457845 on neurons, we performed single-nucleus RNA-Seq (snRNA-Seq) on the spinal cords from $SOD1^{G93A}$ transgenic mice treated with PF-04457845 or unmodified chow (Figure 8A, Supplemental Table S9). Sequencing quality was high, with > 90% of bases at Q30 in the RNA reads, a mean of 50,000 reads per cell, and > 76% of reads mapped to the genome. Unsupervised clustering identified six major cell types, and each cluster expressed cell type-specific cell markers (Figure 8, B and C). The cluster of neurons expressed *Cnr1*, the gene encoding the CB1 receptor; however, *Cnr2*, the CB2 receptor, was barely expressed in the neuronal population (Figure 8, D and E). The administration of PF-04457845 up-regulated the expression of genes including *Tshz3*, *Ppp3r1*, and *Cyfip1* in neurons (Figure 8F). Enrichment analysis revealed that PF-04457845 activates synapse plasticity and neuronal development, although no specific pathway was downregulated with the treatment (Figure 8, G and H). In addition, although the abundance of *Cnr1*-positive neurons was not significantly altered, pathway analysis revealed treatment-associated transcriptional changes in this neuronal subset (Supplemental Figure S15). In oligodendrocytes, pathway analysis revealed treatment-associated changes related to myelination, oligodendrocyte differentiation, and cytoskeletal organization, suggesting transcriptional remodeling without a major change in oligodendrocyte abundance (Figure 5, K and L, Supplemental Figure S16). In microglia, PF-04457845 treatment was associated with downregulation of pathways related to cytokine production, and cytoskeletal/cell migration programs, together with upregulation of pathways related to synapse organization and trans-synaptic signaling (Supplemental Figure S17).

Discussion

In the present study, metabolome and lipid mediator analysis of patients' sera identified metabolic pathways associated with the progression rates of sporadic ALS. Investigation of individual metabolites showed that elevated serum levels of NATs were correlated with longitudinal changes in the ALSFRS-R and associated with shorter survival. Based on these clinical findings, we performed an in vitro screening of compounds that target the identified metabolic pathways. Among the hit compounds in the cellular assay using NSC-34 cells and iPSC-MN derived from ALS patients, PF-04457845, an FAAH inhibitor which up-regulates NATs and NAEs, ameliorated motor neuron degeneration in $SOD1^{G93A}$ transgenic mice, presumably through the regulation of microglial and neuronal function. These findings indicate the elevation of NATs is a progression-related biomarker of sporadic ALS, and manipulation of NAT metabolism, especially inhibition of FAAH, can be a therapeutic strategy.

Based on the data analysis of sporadic ALS patient serum metabolomics, we selected the following five key metabolic pathways that showed differences between rapidly and slowly progressive groups: NAT, purine/xanthine, polyamine/arginine, bile acid, and acylcarnitine metabolism. Previous studies on metabolomics in ALS analyzed the plasma or cerebrospinal fluid (CSF) of patients and healthy individuals, although the results vary due to differences in samples and metabolomic methodologies (36–44). The present study partially reproduced the results of such previous studies. For instance, we identified altered serum levels of adenine, xanthosine, and xanthine in ALS patients. Alterations in purine/xanthine pathways have also been reported in previous studies (40, 42), suggesting that reactive oxygen species (ROS) generated by xanthine oxidase are related to ALS etiology. Our study also demonstrated alterations in the levels of acylcarnitine, a metabolite involved in β-oxidation of fatty acids in mitochondria, which has been reported in previous metabolomic studies (43, 44). Another finding of the present study is altered polyamine/arginine

metabolism in sporadic ALS patients. Our results showed that serum levels of spermidine and (*N*(1) + *N*(8))-acetylspermidine were increased in the rapidly progressive ALS group. A previous report exploring human plasma and SOD1^{G93A} transgenic mice plasma, cerebral cortex, and muscle tissue by metabolomics identified alterations in polyamine metabolism as common metabolic phenotypes of human ALS and SOD1^{G93A} transgenic mice (41). Although sphingolipid metabolism was not prioritized among the candidate pathways identified in our metabolomic analyses, sphingosine-related alterations were also observed in the rapid-versus-slow comparison. This is broadly consistent with prior reports implicating sphingolipid dysregulation in ALS, including *SPTLC1*-associated pathogenesis (45, 46).

The major discovery of the present study is that NATs, lipid mediators that are included in the expanded ECS (35, 47), are up-regulated in sporadic ALS patients with rapid progression. NATs are chiefly produced by conjugation of taurine with fatty acyl chains by bile acid-CoA: amino acid N-acyltransferase (BAAT) in the liver, whereas the biosynthetic pathway of NATs in the central nervous system remains unclear (48). The serum levels of NATs were increased in the rapidly progressive ALS group, being consistent with the result of lipidomics analysis on the spinal cord of SOD1^{G93A} transgenic mice. Furthermore, the serum levels of NATs were closely correlated with the longitudinal decrease in the ALSFRS-R rating and survival in the separate two cohorts, while major endocannabinoids, AEA and 2-AG, were unchanged in subjects with ALS. Although functions of NATs in the central nervous system have yet to be elucidated, our results suggest that NATs are aberrantly regulated in patients and the mouse model of ALS and associated with disease progression in sporadic ALS.

In our cellular experiments, neuroprotective effects of PF-04457845, an inhibitor of FAAH, and *N*-stearoyl taurine, one of NAT species, are stronger than those of AEA or 2-AG, and the effectiveness of PF-04457845 was reproducible in iPS-MN derived from ALS

patients. Moreover, pharmacological inhibition of FAAH led to a substantial increase in the levels of both NATs and NAEs in the spinal cord, resulting in phenotypic amelioration of the mutant SOD1 mice. Collectively, targeting the expanded ECS, including NATs and NAEs, appears to be a common therapeutic approach for both human patients and the animal model of ALS. Our findings also suggest that the elevated levels of NATs in rapidly progressive ALS are indicative of compensatory but insufficient metabolic responses, and that further upregulation of this pathway may mitigate disease progression. PF-04457845 is known to increase the concentration of endocannabinoids in tissues, including those in the central nervous system (49), and has been examined in a phase 2 clinical trial for pain associated with osteoarthritis, which demonstrated the safety and tolerability of this compound in humans (50). Our results thus suggest that PF-04457845 is a candidate for disease-modifying therapy for ALS. Given that NAT synthesis is also linked to hepatic enzyme BAAT (48), regulation of such enzyme may be an alternative potential therapeutic strategy for ALS.

Major molecules of the ECS act through endocannabinoid receptors CB1 and CB2. For instance, NAEs including AEA bind to CB1 and CB2 as well as to transient receptor potential cation channel subfamily V member 1 (TRPV1), while NATs are known as ligands for TRPV1 and TRPV4. In previous studies, activation of the CB1 and CB2 pathways demonstrated potential benefits in $SOD1^{G93A}$ mice (28, 51). The bulk RNA-Seq data and Western blot on the spinal cords from treated mice revealed activation of the IL-13 and CB2 signaling pathways, both of which are known to promote a neuroprotective microglial state (35). It is also known that the activation of TRPV1 regulates microglial lipid metabolism and inflammation (52). The effect of PF-04457845 in our study is, at least partially, attributable to microglia adopting a neuroprotective phenotype, characterized by enhanced anti-inflammatory signaling and lipid metabolic support, as indicated by the increased protein levels of CD36 and LPL which are specifically expressed in microglia. In addition, our study

also demonstrated the benefits of PF-04457845 in NSC-34 cells expressing pathogenic TDP-43 or SOD1 protein and iPS-MN derived from ALS patients, suggesting the effect of this compound on neurons. In support of this view, the results of snRNA-Seq indicated that *Tshz3*, *Cyfip1*, and *Ppp3r1* are up-regulated in neurons treated with PF-04457845 in vivo. Tshz3 is essential for cerebral cortical projection neuron development and has been implicated in the pathogenesis of autism spectrum disorder (ASD) (53). CYFIP1 is also related to ASD and schizophrenia and is known to play an important role in dendritic spine maturation, synaptic activities, and plasticity and acts with CB1 (54–58). Ppp3r1 is a calcineurin subunit that is required for neuronal survival and neurite outgrowth of mesencephalic dopaminergic neurons by glial cell line-derived neurotrophic factor (59). Variants in *PPP3R1* are associated with the accelerated progression of Alzheimer's disease (60). Altogether, in addition to the microglial mechanism mentioned above, PF-04457845 appears to have direct protective effects on neurons via CB1-mediated pathways.

The present study has several limitations. First, the sample size of the clinical study was small, even though we analyzed two separately recruited clinical cohorts. Therefore, larger validation studies are needed. Second, we utilized two murine cellular models for in vitro screening and $SOD1^{G93A}$ transgenic mice for in vivo analysis of motor neurons and glial cells. These models do not necessarily reflect the pathogenesis of sporadic ALS, though our study demonstrated the common elevation of NATs in rapid progressive ALS patients and the murine model. Finally, the efficacy of the FAAH inhibitor PF-04457845 seems superior to similar approaches in the literature, but the pharmacological basis for the difference remains unclear.

Conclusion

Our study suggests that the dysregulation of NATs may serve as a potential biomarker for ALS progression, representing a common therapeutic target in the pathophysiology of both human ALS and an animal model. Furthermore, the FAAH inhibitor PF-04457845, which up-regulates NATs and NAEs in murine spinal cords, emerges as a promising disease-modifying therapy for ALS.

Methods

Sex as a biological variable

The clinical study included both male and female participants. Sex-stratified analyses of *N*-acyl taurine levels revealed similar trends across both sexes. When PF-04457845 treatment was applied to $SOD1^{G93A}$ transgenic mice, consistent improvements in motor function and survival were observed in both male and female mice. Pathological analyses were performed using male $SOD1^{G93A}$ transgenic mice to ensure consistency and sensitivity, as males exhibit a more severe and uniform ALS phenotype (61).

Participants

Subjects who were clinically diagnosed with the revised El Escorial criteria of definite, probable, or possible ALS were consecutively recruited separately for a discovery cohort and a replication cohort. The principal inclusion criteria were no family history and disease duration of $\leq$ 2 years at the time of enrollment. Subjects who had severe complications such as malignancy, heart failure, or renal failure and those with Mini-Mental State Examination (MMSE) score of $\leq$ 23 were excluded from this study. For the discovery cohort, a total of 26 subjects with ALS and 10 healthy controls were analyzed; for the replication cohort, a total of

55 subjects with ALS and 25 healthy controls were analyzed. Subjects with sporadic ALS were assessed during hospitalization at the initial evaluation and follow up evaluations at an outpatient clinic or by telephone were conducted every 6 months in the discovery cohort. In the replicate cohort, the second evaluation was performed 3–11 months after the initial assessment. Age- and sex-matched healthy controls were also recruited during the same period as the ALS patients. All study subjects were Japanese and observed at the Nagoya University Hospital between May 2013 and June 2025.

Clinical evaluation and sample collection

Disease onset was defined as the time point when the subject felt weakness of any body part. Patients with ALS were classified according to onset type and were sorted into either the limb-onset type group or the bulbar-onset type group, according to the site where they first felt weakness. Disease severity was assessed with the Japanese version of the revised ALS Functional Rating Scale (ALSFRS-R), a validated questionnaire-based functional rating scale for ALS (62). The introduction of tracheostomy positive pressure ventilation (TPPV) or death of the patient was defined as the primary endpoint.

At the first evaluation, venous blood samples were collected from ALS patients in the supine position after more than 12 hours of fasting and just after waking up during hospitalization. At the outpatient clinic, venous blood samples of healthy individuals in the sitting or supine position were collected after more than 12 hours of fasting. Serum samples were centrifuged at 3000 rpm for 10 min and stored at –80 °C until processing at Metabolon Inc. and Shimadzu Techno-Research, Inc.

Metabolomics analysis

Untargeted metabolomics profiling of serum samples was performed using ultrahigh-performance liquid chromatography-tandem mass spectrometry (UPLC–MS/MS) by

Metabolon, inc. To remove protein, dissociate small molecules bound to protein or trapped in the precipitated protein matrix and to recover chemically diverse metabolites, proteins were precipitated with methanol. The resulting extract was divided for analysis by two separate reversed-phase (RP)/UPLC–MS/MS methods with positive ion mode electrospray ionization (ESI), for analysis by RP/UPLC–MS/MS with negative ion mode ESI, and for analysis by HILIC/UPLC–MS/MS with negative ion mode ESI. Compounds were identified by comparison to the library entries of purified standards or recurrent unknown entities, and relative levels were quantitated. Missing values were replaced by the minimal value determined for that metabolite in the entire cohort, per Metabolon protocols.

Lipid mediator analysis

To validate the alterations in *N*-acyl taurines observed in the discovery cohort, lipid mediators in serum samples from the replication cohort were measured and compared using LC-MS/MS by Shimadzu Techno-Research, Inc. Sample preparation was performed according to the Shimadzu lipid mediator method package. Missing values were imputed with the minimum detected value for each metabolite across the entire cohort, and metabolites for which more than 50% of the values were below the limit of detection were excluded from the analysis.

Metabolomics data analysis

Volcano plots, one-way ANOVA, heatmap analysis, and enrichment analysis were performed using MetaboAnalyst 6.0 (63). For multivariate analysis, sparse partial least squares discriminant analysis (sPLS-DA) was performed to discriminate between rapid ALS patients, slow ALS patients and healthy individuals using MetaboAnalyst 6.0. Loading plots indicated the importance of metabolites for sPLS-DA. Adding to this multivariate analysis, random forest (RF) classification in R software was applied to determine whether the differences in the

identified metabolites effectively separated the three groups. The mean decrease in accuracy, which represents variable importance, was calculated.

ALS cellular models, cell culture, and transfection

Mouse NSC-34 motor neuron-like cells (kindly provided by N.R. Cashman, University of British Columbia, Vancouver, Canada) were cultured in a humidified atmosphere of 95% air/5% CO2 in a 37 °C incubator. NSC-34 cells were maintained in Dulbecco's Modified Eagle's Medium (DMEM) containing 10% (v/v) fetal bovine serum (Life Technologies) with 1% penicillin/streptomycin (Wako). The plasmids were transfected by using OPTI-MEM (Gibco) and Lipofectamine 2000 (Invitrogen) according to the manufacturer's instructions. NSC-34 cells were differentiated in DMEM for 48 hours. We prepared the mutant TDP-43^{A315T} and the mutant SOD1^{G93A} vectors as previously described (64, 65). As for TDP-43, site-specific mutagenesis was performed as described previously using the following primers: F: acgttcagcattaatccagccatgatg R: accaaagttcatcccaccacccatattactac.

hiPSC culture and differentiation in vitro

The experiments were performed as described previously (66–68). Briefly, hiPSCs derived from three ALS patients and a healthy individual (HPS0736, 0760, 0896 and 0063 obtained from the RIKEN BioResource Research Center (Tsukuba, Japan) (69, 70)) were maintained on feeder cells with human embryonic stem cell medium. For differentiation, hiPSC colonies were detached and embryoid bodies were generated by human embryoid body medium with LDN, SB, CHIR, retinoic acid, and purmorphamine for 14 days. Embryoid bodies were dissociated into single cells using TrypLE Select and were plated on dishes coated with growth factor reduced Matrigel at a density of 2×10^5 cells/cm^2. Motor neurons were cultured in motor neuron medium consisting of B27 supplement, CultureOne supplement, non-essential amino acid, retinoic acid, purmorphamine, cyclic AMP, recombinant brain-derived neurotrophic

512 factor, recombinant glial cell line derived neurotrophic factor, recombinant human insulin-like
513 growth factor-1, and L-ascorbic acid for up to three weeks. Half of the medium was changed
514 every 2–3d.

515 PF-04457845 was administered at 0 nM, 20 nM and 40 nM to motor neurons cultured for 2
516 weeks. The number of cell cluster and neurite length were evaluated by IncuCyteSX5® live-
517 cell imaging system (Essen Bioscience) on day 7 after drug administration. Cell clusters and
518 neurite length were assessed using the NeuroTrack analysis algorithm. LDH release was also
519 assessed as the drug efficacy.

520 **Chemical compounds**

521 PF-04457845 was supplied by Mitsubishi-Tanabe Pharma (Yokohama, Japan), and the other
522 compounds were commercially purchased from Cayman Chemical (arvanil, N-oleoyl taurine,
523 N-stearoyl taurine, N-palmitoyl taurine); Kanto Chemical (xanthine); MedChemExpress
524 (eflornithine); Focus Bioscience (Mitoquazone); Sigma–Aldrich (allantoin, arachidonoyl
525 ethanolamide, clofibrate, febuxostat, inosine, metformin, MDL72527, oleic acid, riboflavin, S-
526 adenosyl-L-methionine, Spermidine, Spermine, and 2-arachidonoyl glycerol); TCI, (agmatine,
527 glicocholic acid, glycoursodeoxycholic acid, riluzole, theobromine, theophiline, trimetazidine,
528 and xanthosine), Matrix Scientific (edaravone), or Wako (arginine and ornithine).

529 **Cell viability and toxicity assay**

530 Cell viability assays were performed using a WST-8 kit (Dojindo) according to the
531 manufacturer's instructions. Transfected and differentiated NSC-34 cells were cultured in 96-
532 well plates, and chemical compounds were administered. Twenty-four hours after treatment
533 with the selected chemicals, cells were incubated with the WST-8 substrate for 30–60 min,
534 after which the absorbance of the wells was measured at 450 nm using a plate reader
535 (EnSpireTM, PerkinElmer). Toxicity assays were performed using the Cytotoxicity Detection

Kit PLUS (Roche Diagnostics). Twenty-four hours after treating the cells, the medium was incubated with the substrate for 15 min and spectrophotometrically assayed at 492 nm using a plate reader.

Preclinical murine model of ALS

Transgenic mice overexpressing the human SOD1 gene carrying the G93A mutation were purchased from the Jackson Laboratory (Bar Harbor, Maine, USA) and maintained as hemizygotes by mating transgenic males with B6/SJL F1 females. The $SOD1^{G93A}$ transgenic mice were randomly allocated to PF-04457845-treated (n = 28; male n = 13, female n = 15), or untreated groups (n = 34; male n = 17, female n = 17), according to the guidelines for preclinical animal research in ALS/MND (71). For oral administration of PF-04457845, PF-04457845 was mixed with powdered rodent chow at a concentration of 0.001%, which is consistent with the dose of 1 mg/kg/day. All mice were placed under a 12-h light/12-h dark cycle in a temperature- and humidity-controlled facility and had unlimited access to food and water. PF-04457845 (1 mg/kg/day) was administered from week 8 until the ethical endpoint, which was defined as loss of the ability to right itself after being placed on its side or inability to ambulate from a given location. The endpoint was evaluated daily. PF-04457845 was also administered to wild-type C57BL/6 and B6/SJL mice to assess possible nonspecific effects on body weight and motor performance. In C57BL/6 mice, each group included 10 animals (male, n = 5; female, n = 5), whereas in B6/SJL mice, each group included 9 animals (male, n = 5; female, n = 4).

Behavioral analysis

All behavioral tests were performed weekly, and the data were prospectively analyzed. The animal rotarod performances were assessed weekly using an Economex Rotarod during the light phase of the 12-hr light/12-hr dark cycle as described previously (72) (Ugo Basile). We

performed three trials and recorded the longest duration on the rod for every mouse in a randomized order. We stopped the timer when the mouse fell from the rod or after a maximum of 180 seconds. The grip strength was measured with a Grip Strength Meter (MK-380M, Muromachi Kikai). Behavioral analysis was performed by two evaluators blind to the treatment. To impute values of mice after death, the final body weights of all mice were carried forward when calculating group mean values as described in a previous report (72). The values of grip strength and rotarod performance after death were imputed to zero.

Animal sample collection

Male mice were deeply anesthetized, and the entire spinal cord was dissected and snap-frozen in powdered CO_2 in acetone for Western-blot and RNA-Seq and by liquid nitrogen for lipidome analysis. The mice were sacrificed at the age of 16 weeks. Mouse tissues were dissected, postfixed with 10% phosphate-buffered formalin and paraffin embedded for histological analysis.

Immunoblotting

Mouse tissues were lysed with RIPA buffer (50 mM 1 M Tris pH 7.4, 150 mM NaCl, 1% Triton X-100, 1% deoxycholate, 0.1% SDS) using a dounce homogenizer for mouse tissue, sonicated, and centrifuged at 20,000 × g for 15 min at 4 °C. The supernatant was kept as the RIPA soluble fraction, and equal amounts of protein were separated on 5–20% SDS–PAGE gels (Wako) and transferred to Hybond-P membranes (GE Healthcare). The following primary antibodies and dilutions were utilized: SOD1 (ab51254, 1:1000; Abcam), IBA-1 (016-20001, 1:1000; Wako), CD36 (ab252923, 1:1000; Abcam), CD86 (#1858-1, 1:1000; Epitomics), LPL (GTX101125, 1:1000; GeneTex), p44/42 MAPK (#9102, 1:5000; CST), and phosphorylated p44/42 MAPK (#5726, 1:1000; CST). Primary antibodies bound to the proteins were probed with a 1:5000 dilution of horseradish peroxidase-conjugated secondary antibodies, and the bands were

584 detected using an immunoreaction enhancing solution (Can Get Signal; Toyobo) and enhanced
585 chemiluminescence (ECL Prime; GE Healthcare). Chemiluminescence signals were digitized
586 using a LAS-3000 imaging system (Fujifilm). The signal intensities of independent blots were
587 quantified using ImageJ. Membranes were reprobed with an anti-GAPDH antibody (MAB374,
588 1:5000; Millipore) for normalization.

589 **Histology and immunohistochemistry**

590 The lumbar spinal cords were collected from mice. The samples were embedded in paraffin,
591 and 3-μm sections were prepared. Sections designated for anti-ChAT, GFAP, and IBA-1, and
592 SOX10 staining were boiled in 10 mM citrate buffer for 15 min for antigen retrieval, incubated
593 overnight with the respective primary antibodies, and then incubated with a secondary antibody
594 labeled with a polymer as part of the Envision+ system containing horseradish peroxidase
595 (Dako Cytomation). The following primary antibodies and dilutions were used to stain mouse
596 tissues: ChAT (AB144P, 1:100; Millipore), GFAP (#ab53554, 1:1000; Abcam), IBA-1 (013-
597 27691, 1:1000; Wako) and SOX10 (sc-365692, 1:500; Santa Cruz Biotechnology).

598 ChAT-immunoreactive neurons in the ventral horn of the lumbar spinal cord were counted in
599 every fifth section from the 50 consecutive sections by using BZ-X810 (Keyence), and the
600 mean total number of ChAT-immunoreactive neurons was compared between treatment groups.
601 ChAT-immunoreactive neuronal area and GFAP- and IBA-1-positive areas were quantified
602 using NIH ImageJ software, and SOX10-positive cells were counted.

603 **Lipidomics analysis of murine spinal cords**

604 Frozen tissues (about 10 mg) were homogenized with a probe sonicator in methanol/water =
605 2/0.7 (v/v), and lipids were extracted using the method of Bligh and Dyer with internal
606 standards. The organic (lower) phase was transferred to a clean vial and dried under a nitrogen
607 stream. The lipids were resolubilized in methanol/isopropanol/chloroform = 45/45/10 (v/v/v)

and stored at -80 °C. A portion of the extracted lipids was injected into an ultrahigh-performance liquid chromatography (LC)-electrospray ionization (ESI)–tandem mass spectrometry system (LC-MS/MS). The quantification of FFA was carried out as described previously (73). For the quantification of Sulfatide, S1P, NAT, NAEP, LPA, LPG, LPI, LPS, PA, PS, and PT, LC separation was performed on an ACQUITY Premier BEH C18 column (1.7 μm, 2.1 × 50 mm; Waters). Mobile phase A was H_2O/methanol = 95/5 (v/v%), mobile phase B was isopropanol/methanol = 63/37 (v/v%), and mobile phase C was H_2O/methanol/28% NH_4OH = 93/5/2 (v/v/v%). The LC method consisted of a linear gradient from A/C = 95/5 (v/v%) to B/C = 95/5 (v/v%) over 15 min, B/C = 95/5 (v/v%) for 8 min, and equilibration with A/C = 95/5 (v/v%) for 5 min (28 min total run time). The flow rate was 0.3 mL/min, and the column temperature was 25 °C. For the quantification of BMP, an isocratic LC separation was performed with methanol containing 10 mM ammonium formate on a COSMOCORE 2.6C18 column (2.1 × 100 mm; Nacalai Tesque) coupled to an ACQUITY UPLC BEH C18 VanGuard Pre-column (1.7 μm, 2.1 × 5 mm; Waters, Milford, MA, USA). The flow rate was 0.3 mL/min, and the column temperature was 55 °C. For the quantification of other lipid classes, LC separation was performed on an ACQUITY UPLC BEH C18 column (1.7 μm, 2.1 × 100 mm; Waters) coupled to an ACQUITY UPLC BEH C18 VanGuard Pre-column (1.7 μm, 2.1 × 5 mm; Waters). Mobile phase A was acetonitrile/water = 60/40 (v/v%) containing 10 mM ammonium formate and 0.1% (v/v) formic acid, and mobile phase B was isopropanol/acetonitrile = 90/10 (v/v%) containing 10 mM ammonium formate and 0.1% (v/v) formic acid. The LC gradient consisted of 20% B for 2 min, a linear gradient to 60% B over 4 min, a linear gradient to 100% B over 16 min, and equilibration with 20% B for 5 min (27 min total run time). The flow rate was 0.3 mL/min, and the column temperature was 55 °C. Multiple reaction monitoring (MRM) was performed using a Xevo TQ-S micro triple quadrupole mass spectrometry system (Waters) equipped with an ESI source. The ESI capillary voltage was set

at 1.0 kV, and the sampling cone was set at 30 V. The source temperature was 150 °C, the desolvation temperature was 500 °C, and the desolvation gas flow was 1,000 L/h. The cone gas flow was 50 L/h.

Lipidomics data analysis

Detailed methods are provided in the Supplemental Methods.

RNA-Seq of murine spinal cords

Detailed methods are provided in the Supplemental Methods.

RNA-Seq data analysis

Detailed methods are provided in the Supplemental Methods.

Single-nucleus RNA-Seq of murine spinal cords

Nuclei isolation: Detailed methods are provided in the Supplemental Methods.

Single-nucleus RNA sequencing: The nuclei per sample were run on the 10× Chromium Single cell 3' gene expression v3.1 platform. Sequencing libraries were constructed according to the manufacturer's instructions, and cDNA samples were run on an Agilent Bioanalyzer using the High Sensitivity DNA Chip as quality control and determination of cDNA concentrations. The samples were run on an Illumina HiSeq2500 at Read 1 = 28 bp and Read 2 = 90 bp, with a minimum depth of 20,000 reads per nucleus. For alignment, introns and exons were included in the reference genome (mm10) using the CellRanger v.6.1.2 pipeline (10X Genomics). Sequencing data were analyzed using the R package Seurat Version 4.1.3. The gene barcode matrices for each sample were imported into R using the Read10X function.

Quality check analysis: All 10 x runs for each sample were filtered for nuclei with less than 1% contamination of mitochondrial genes, with 200 to 2000 genes per cell, and genes with a

count of 1 in at least 3 cells were retained. A total of 4,869 nuclei passed quality control filtering and proceeded to analysis. UMI counts were then normalized in Seurat 3.0, and the top 2000 highly variable genes were identified using the FindVariableFeatures function with variance stabilization transformation (VST).

Clustering and data analysis: Principal component analysis (PCA) was performed using the top 2000 variable genes prior to clustering. To visualize profiles in two-dimensional space, t-distributed stochastic neighbor embedding (t-SNE) was performed with the top 25 principal components based on ElbowPlot. Clustering was performed using the FindNeighbors and FindClusters functions in the Seurat R package, and the resolution was 0.15. To identify each cell type, 'Celf4' and 'Rbfox' were used as specific cell markers for neurons, 'Mbp" and 'Mag" for oligodendrocytes, 'Tnr' and 'Vcan" for oligodendrocyte precursor cells (OPCs), 'Ly86' and 'Runx1' for microglia, 'Alp1a2' and 'Aqp4' for astrocytes, and 'Neb' and 'Ttn' for muscular cells. These markers were used to assign cell-type annotations manually for each cell cluster.

Single-nucleus RNA-seq data analysis

DEGs between PF-04457845-treated and untreated groups were identified using the FindMarkers function of the Seurat package in R, using the Wilcoxon rank-sum test. Average log2 (fold change) of gene expression, the percentage of cells expressing the genes in each group (pct.1 and pct.2), *p* value and adjusted *p* value were generated. For the neuronal analysis, DEG lists were produced by filtering all genes for log2-fold changes > 0.1 and adjusted $p < 0.05$. For oligodendrocytes, genes with adjusted $p < 0.05$ were extracted and then separated into upregulated and downregulated genes according to the direction of fold change. For microglia and cannabinoid receptor 1 (CB1)-positive neurons, genes with $p < 0.05$ were used for downstream pathway analysis. Ontology terms with a *p*-value < 0.01, a minimum count of

3, and an enrichment factor > 1.5 were extracted. DEGs up-regulated in PF-04457845-treated mice compared to untreated mice were analyzed with the Metascape portal (www.metascape.org)(74).

Statistical analysis

We analyzed the data by using two-sided unpaired *t* tests and chi-square tests for comparisons of two groups and analysis of variance (ANOVA) for multiple comparisons. For multiple comparisons, we utilized Tukey's test for comparing metabolites among Rapid ALS patients, Slow ALS patients, and healthy individuals and Dunnett's test was used to compare each concentration of chemical compounds with baseline in ALS cell models. Data from iPSC-derived motor neurons were analyzed using a mixed-effects model with treatment as a fixed effect and iPSC line as a random effect, followed by Dunnett's multiple-comparisons test. ALSFRS-R slope values were transformed using the Yeo–Johnson transformation. A Spearman rank correlation test was performed to analyze the correlation between ALSFRS-R slope and serum metabolite levels. In addition, survival was analyzed using Kaplan–Meier and log-rank tests for comparison of rapidly progressive ALS patients and slowly progressive ALS patients. The same methods were also used to compare untreated and PF-04457845-treated $SOD1^{G93A}$ transgenic mice. Body weight, grip strength, and rotarod test in mice were analyzed using two-way ANOVA. We considered p values of < 0.05 to indicate statistical significance, and a correlation coefficient value (r) of 0.40–0.59 is considered moderate, while 0.60–0.79 is considered strong in Spearman's rank correlation coefficient. For experiments using mice, the number of animals is stated in the figure legends. All statistical analyses were performed using R (version 4.5.2) and GraphPad Prism 10.

Ethics approval and consent to participate

The clinical part of this study was conducted according to the Declaration of Helsinki, the Ethical Guidelines for Medical and Health Research Involving Human Subjects endorsed by the Japanese government. It was approved by the Ethics Review Committee of Nagoya University Graduate School of Medicine (Nos. 2013-0035 and 2015-0041), and all participants gave written informed consent before participation.

All animal experiments were performed in accordance with the National Institutes of Health Guide for the Care and Use of Laboratory Animals, ARRIVE guideline and under the approval of the Nagoya University Animal Experiment Committee (No. 29170).

Generative artificial intelligence

ChatGPT (GPT-5.4; OpenAI) was used solely for correction of typographical errors and minor grammatical issues. All revisions were reviewed and approved by the authors. The use of this AI tool occurred on 6th April 2026.

Availability of data and materials

The metabolomics source data were deposited into Mendeley (doi:10.17632/f8gtkwfs6s.1). The snRNA-Seq and bulk RNA-Seq raw data files have been deposited into the NCBI Gene Expression Omnibus (GEO) under accession number GSE242942 and are publicly available at : https://www.ncbi.nlm.nih.gov/geo/query/acc.cgi?acc=GSE242942
Supporting data values for all graphs in the main manuscript and supplemental material are provided in an accompanying Excel file.

Funding

This work was partly supported by JSPS KAKENHI (JP21K15677 and JP23K14773 to DI; JP20H00527 and JP23H00420 to MK) and AMED (JP21wm0425013, JP22nk0101575,

JP22am0401007, and JP24wm0625301 to MK; JP21wm0425008 to TY; and JP23bm1423006 to SY). This work was also supported by Mitsubishi-Tanabe Pharma.

Authors' contributions:

Conceptualization: DI, MI, YI, AH, MK. Methodology: DI, MI, YI, AH, MK. Clinical investigation: DI, AH, SY, YK, SK. Molecular experiments: DI, MI, SN, SY. Lipidomics; HCLO, TY. Single nucleus RNA-Seq: MI, TA, KH. Scientific discussions: KO, TS, YT, MN, YO, JN, GS, ST, KT. Supervision: MI, YI, MK. Writing–original draft: DI. Writing–review & editing: MI, YI, MK.

Acknowledgements

We thank all the members of Department of Neurology, Nagoya University Graduate School of Medicine, for their helpful discussion on the project, all the members of Division of Experimental Animals, Nagoya University Graduate School of Medicine, for their care and maintenance of the experimental mice and Division for Medical Research Engineering, Nagoya University Graduate School of Medicine, for usage of FACSAria Fusion and IncuCyte SX5®.

References

1. Yokoseki A, et al. TDP-43 mutation in familial amyotrophic lateral sclerosis. *Ann Neurol*. 2008;63(4):538–542.

2. Sreedharan J, et al. TDP-43 mutations in familial and sporadic amyotrophic lateral sclerosis. *Science*. 2008;319(5870):1668–1672.

3. Kabashi E, et al. TARDBP mutations in individuals with sporadic and familial amyotrophic lateral sclerosis. *Nat Genet*. 2008;40(5):572–574.

4. Gitcho MA, et al. TDP-43 A315T mutation in familial motor neuron disease. *Ann Neurol*. 2008;63(4):535–538.

5. Renton AE, et al. A hexanucleotide repeat expansion in C9ORF72 is the cause of chromosome 9p21-linked ALS-FTD. *Neuron*. 2011;72(2):257–268.

6. DeJesus-Hernandez M, et al. Expanded GGGGCC Hexanucleotide Repeat in Noncoding Region of C9ORF72 Causes Chromosome 9p-Linked FTD and ALS. *Neuron*. 2011;72(2):245–256.

7. Rosen DR, et al. Mutations in Cu/Zn superoxide dismutase gene are associated with familial amyotrophic lateral sclerosis. *Nature.* 1993;362(6415):59–62.

8. Wijesekera L, Leigh P. Amyotrophic lateral sclerosis. *Orphanet J Rare Dis*. 2009;4:3.

9. Rowland LPL, Shneider NNA. Amyotrophic Lateral Sclerosis. *N Engl J Med*. 2001;344(22):1688–1700.

10. Mitsumoto H, et al. Clinical trials in amyotrophic lateral sclerosis: Why so many negative trials and how can trials be improved? *Lancet Neurol*. 2014;13(11):1127–1138.

11. Petrov D, et al. ALS clinical trials review: 20 years of failure. Are we any closer to registering a new treatment? *Front Aging Neurosci*. 2017;9:68.

12. Bensimon G, et al. A Controlled Trial of Riluzole in Amyotrophic Lateral Sclerosis. *N Engl J Med*. 1994;330(9):585–591.

13. Writing Group; Edaravone (MCI-186) ALS 19 Study Group. Safety and efficacy of edaravone in well defined patients with amyotrophic lateral sclerosis: a randomised, double-blind, placebo-controlled trial. *Lancet Neurol*. 2017;16(7):505–512.

14. Baxi EG, et al. Answer ALS, a large-scale resource for sporadic and familial ALS combining clinical and multi-omics data from induced pluripotent cell lines. *Nat Neurosci*. 2022;25(2):226–237.

15. Imamura K, et al. The Src/c-Abl pathway is a potential therapeutic target in amyotrophic lateral sclerosis. *Sci Transl Med*. 2017;9(391):eaaf3962.

16. Fujimori K, et al. Modeling sporadic ALS in iPSC-derived motor neurons identifies a potential therapeutic agent. *Nat Med*. 2018;24(10):1579–1589.

17. Van Harten ACM, et al. Non-cell-autonomous pathogenic mechanisms in amyotrophic lateral sclerosis. *Trends Neurosci*. 2021;44(8):658–668.

18. Boillée S, et al. Onset and Progression in Inherited ALS Determined by Motor Neurons and Microglia. *Science*. 2006;312(5778):1389–1392.

19. Yamanaka K, et al. Astrocytes as determinants of disease progression in inherited amyotrophic lateral sclerosis. *Nat Neurosci*. 2008;11(3):251–253.

20. Li J, et al. Neuronal TDP-43 regulates myelin formation via neurexin 1 mRNA stabilization. *Proc Natl Acad Sci U S A*. 2026;123(9):e2513642123.

21. Bouteloup C, et al. Hypermetabolism in ALS patients: An early and persistent phenomenon. *J Neurol*. 2009;256(8):1236–1242.

22. Steyn FJ, et al. Hypermetabolism in ALS is associated with greater functional decline and shorter survival. *J Neurol Neurosurg Psychiatry*. 2018;89(10):1016–1023.

23. Nakamura R, et al. Ideal body weight-based determination of minimum oral calories beneficial to function and survival in ALS. *Front Neurol*. 2023;14:1286153.

24. Mariosa D, et al. Blood biomarkers of carbohydrate, lipid, and apolipoprotein metabolisms and risk of amyotrophic lateral sclerosis: A more than 20-year follow-up of the Swedish AMORIS cohort. *Ann Neurol*. 2017;81(5):718–728.

25. Araki K, et al. TDP-43 regulates early-phase insulin secretion via CaV1.2-mediated exocytosis in islets. *J Clin Invest*. 2019;129(9):3578–3593.

26. Ludolph AC, et al. Effect of High-Caloric Nutrition on Survival in Amyotrophic Lateral Sclerosis. *Ann Neurol*. 2020;87(2):206–216.

27. Wills AM, et al. Hypercaloric enteral nutrition in patients with amyotrophic lateral sclerosis: A randomised, double-blind, placebo-controlled phase 2 trial. *Lancet*. 2014;383(9934):2065–2072.

28. Bilsland LG, et al. Increasing cannabinoid levels by pharmacological and genetic manipulation delays disease progression in SOD1 mice. *FASEB J*. 2006;20(7):1003–1005.

29. Grajchen E, et al. CD36-mediated uptake of myelin debris by macrophages and microglia reduces neuroinflammation. *J Neuroinflammation*. 2020;17(1):224.

30. Zhou W, et al. TREM2-dependent activation of microglial cell protects photoreceptor cell during retinal degeneration via PPARγ and CD36. *Cell Death Dis*. 2024;15(8):623.

31. Paolicelli RC, et al. Microglia states and nomenclature: A field at its crossroads. *Neuron*. 2022;110(21):3458–3483.

32. Traetta ME, et al. Fundamental Neurochemistry Review: Lipids across microglial states. *J Neurochem*. 2025;169(1):e16259.

33. Mecha M, et al. Endocannabinoids drive the acquisition of an alternative phenotype in microglia. *Brain Behav Immun*. 2015;49:233–245.

34. Tanaka M, et al. Endocannabinoid Modulation of Microglial Phenotypes in Neuropathology. *Front Neurol*. 2020;11:87.

35. Cristino L, et al. Cannabinoids and the expanded endocannabinoid system in neurological disorders. *Nat Rev Neurol*. 2020;16(1):9–29.

36. Blasco H, et al. Metabolomics in amyotrophic lateral sclerosis: How far can it take us? *Eur J Neurol*. 2016;23(3):447–454.

37. Blasco H, et al. 1H-NMR-Based metabolomic profiling of CSF in early amyotrophic lateral sclerosis. *PLoS One*. 2010;5(10):e13223.

38. Blasco H, et al. Metabolomics in cerebrospinal fluid of patients with amyotrophic lateral sclerosis: an untargeted approach via high-resolution mass spectrometry. *J Proteome Res*. 2013;12(8):3746–3754.

39. Blasco H, et al. Untargeted 1H-NMR metabolomics in CSF Toward a diagnostic biomarker for motor neuron disease. *Neurology.* 2014;82(13):1167–1174.

40. Veyrat-durebex C, et al. Metabo-lipidomics of Fibroblasts and Mitochondrial-Endoplasmic Reticulum Extracts from ALS Patients Shows Alterations in Purine, Pyrimidine, Energetic, and Phospholipid Metabolisms. *Mol Neurobiol.* 2019;56(8):5780–5791.

41. Patin F, et al. Omics to Explore Amyotrophic Lateral Sclerosis Evolution: the Central Role of Arginine and Proline Metabolism. *Mol Neurobiol*. 2017;54(7):5361–5374.

42. Lee H, et al. Multi-omic analysis of selectively vulnerable motor neuron subtypes implicates altered lipid metabolism in ALS. *Nat Neurosci*. 2021;24(12):1673–1685.

828 43. Goutman SA, et al. Metabolomics identifies shared lipid pathways in independent amyotrophic lateral
829 sclerosis cohorts. *Brain*. 2022;145(12):4425–4439.
830 44. Goutman SA, et al. Untargeted metabolomics yields insight into ALS disease mechanisms. *J Neurol*
831 *Neurosurg Psychiatry.* 2020;91(12):1329–1338.
832 45. Mohassel P, et al. Childhood amyotrophic lateral sclerosis caused by excess sphingolipid synthesis. *Nat*
833 *Med*. 2021;27(7):1197–1204.
834 46. Lone MA, et al. SPTLC1 variants associated with ALS produce distinct sphingolipid signatures through
835 impaired interaction with ORMDL proteins. *J Clin Invest*. 2022;132(18):e161908.
836 47. Grevengoed TJ, et al. N-acyl taurines are endogenous lipid messengers that improve glucose homeostasis.
837 *Proc Natl Acad Sci U S A*. 2019;116(49):24770–24778.
838 48. Trammell SAJ, et al. Identification of bile acid-CoA:amino acid N-acyltransferase as the hepatic N-acyl
839 taurine synthase for polyunsaturated fatty acids. *J Lipid Res*. 2023;64(9):100361.
840 49. Ahn K, et al. Mechanistic and pharmacological characterization of PF-04457845: A highly potent and
841 selective fatty acid amide hydrolase inhibitor that reduces inflammatory and noninflammatory pain. *J*
842 *Pharmacol Exp Ther*. 2011;338(1):114–124.
843 50. Huggins JP, et al. An efficient randomised, placebo-controlled clinical trial with the irreversible fatty
844 acid amide hydrolase-1 inhibitor PF-04457845, which modulates endocannabinoids but fails to induce
845 effective analgesia in patients with pain due to osteoarthritis of the knee. *Pain*. 2012;153(9):1837–1846.
846 51. Pasquarelli N, et al. Evaluation of monoacylglycerol lipase as a therapeutic target in a transgenic mouse
847 model of ALS. *Neuropharmacology*. 2017;124:157–169.
848 52. Sha X, et al. The TRPV1-PKM2-SREBP1 axis maintains microglial lipid homeostasis in Alzheimer's
849 disease. *Cell Death Dis*. 2025;16(1):14.
850 53. Caubit X, et al. TSHZ3 deletion causes an autism syndrome and defects in cortical projection neurons.
851 *Nat Genet*. 2016;48(11):1359–1369.
852 54. Monday HR, et al. Cb1-receptor-mediated inhibitory ltd triggers presynaptic remodeling via protein
853 synthesis and ubiquitination. *Elife*. 2020;9:e54812.
854 55. Cioni JM, et al. Axon-Axon Interactions Regulate Topographic Optic Tract Sorting via CYFIP2-
855 Dependent WAVE Complex Function. *Neuron*. 2018;97(5):1078–1093.e6.
856 56. Hsiao K, et al. Cyfip1 regulates presynaptic activity during development. *J Neurosci*. 2016;36(5):1564–

857 1576.
858 57. DeRubeis S, et al. CYFIP1 coordinates mRNA translation and cytoskeleton remodeling to ensure proper
859 dendritic Spine formation. *Neuron*. 2013;79(6):1169–1182.
860 58. Davenport EC, et al. Autism and Schizophrenia-Associated CYFIP1 Regulates the Balance of Synaptic
861 Excitation and Inhibition. *Cell Rep*. 2019;26(8):2037–2051.e6.
862 59. Consales C, et al. GDNF signaling in embryonic midbrain neurons in vitro. *Brain Res*. 2007;1159:28–
863 39.
864 60. Peterson D, et al. Variants in PPP3R1 and MAPT are associated with more rapid functional decline in
865 Alzheimer's disease: The Cache County Dementia Progression Study. *Alzheimers Dement*. 2014;10(3):366–
866 371.
867 61. Pfohl SR, et al. Characterization of the Contribution of Genetic Background and Gender to Disease
868 Progression in the SOD1 G93A Mouse Model of Amyotrophic Lateral Sclerosis: A Meta-Analysis. *J*
869 *Neuromuscul Dis*. 2015;2(2):137–150.
870 62. Ohashi Y, et al. Study of functional rating scale for amyotrophic lateral sclerosis: revised
871 ALSFRS(ALSFRS-R) Japanese version. *No To Shinkei*. 2001;53(4):346–355.
872 63. Pang Z, et al. MetaboAnalyst 5.0: Narrowing the gap between raw spectra and functional insights.
873 *Nucleic Acids Res*. 2021;49(W1):W388–W396.
874 64. Niwa J, et al. Disulfide bond mediates aggregation, toxicity, and ubiquitylation of familial amyotrophic
875 lateral sclerosis-linked mutant SOD1. *J Biol Chem.* 2007;282(38):28087–28095.
876 65. Iguchi Y, et al. Oxidative stress induced by glutathione depletion reproduces pathological modifications
877 of TDP-43 linked to TDP-43 proteinopathies. *Neurobiol Dis*. 2012;45(3):862–870.
878 66. Yokoi S, et al. The SYNGAP1 3'UTR Variant in ALS Patients Causes Aberrant SYNGAP1 Splicing and
879 Dendritic Spine Loss by Recruiting HNRNPK. *J Neurosci*. 2022;42(47):8881–8896.
880 67. Shimojo D, et al. Rapid, efficient, and simple motor neuron differentiation from human pluripotent stem
881 cells. *Mol Brain*. 2015;8(1):79.
882 68. Onodera K, et al. Unveiling synapse pathology in spinal bulbar muscular atrophy by genome-wide
883 transcriptome analysis of purified motor neurons derived from disease specific iPSCs. *Mol Brain*.
884 2020;13(1):18.
885 69. Takahashi K, et al. Induction of Pluripotent Stem Cells from Adult Human Fibroblasts by Defined Factors.

886 Cell. 2007;131(5):861–872.
887 70. Okita K, et al. An efficient nonviral method to generate integration-free human-induced pluripotent stem
888 cells from cord blood and peripheral blood cells. Stem Cells. 2013;31(3):458–466.
889 71. Ludolph AC, et al. Guidelines for preclinical animal research in ALS/MND: A consensus meeting.
890 *Amyotroph Lateral Scler*. 2010;11(1–2):38–45.
891 72. Hirunagi T, et al. Exercise attenuates polyglutamine-mediated neuromuscular degeneration in a mouse
892 model of spinal and bulbar muscular atrophy. *J Cachexia Sarcopenia Muscle*. 2024;15(1):159–172.
893 73. Lee-Okada HC, et al. Development of a liquid chromatography-electrospray ionization tandem mass
894 spectrometric method for the simultaneous analysis of free fatty acids. *J Biochem*. 2021;170(3):389–397.
895 74. Zhou Y, et al. Metascape provides a biologist-oriented resource for the analysis of systems-level datasets.
896 *Nat Commun*. 2019;10(1):1523.

Figure legends

Figure 1. Metabolomics analysis of patients with ALS and healthy individuals.

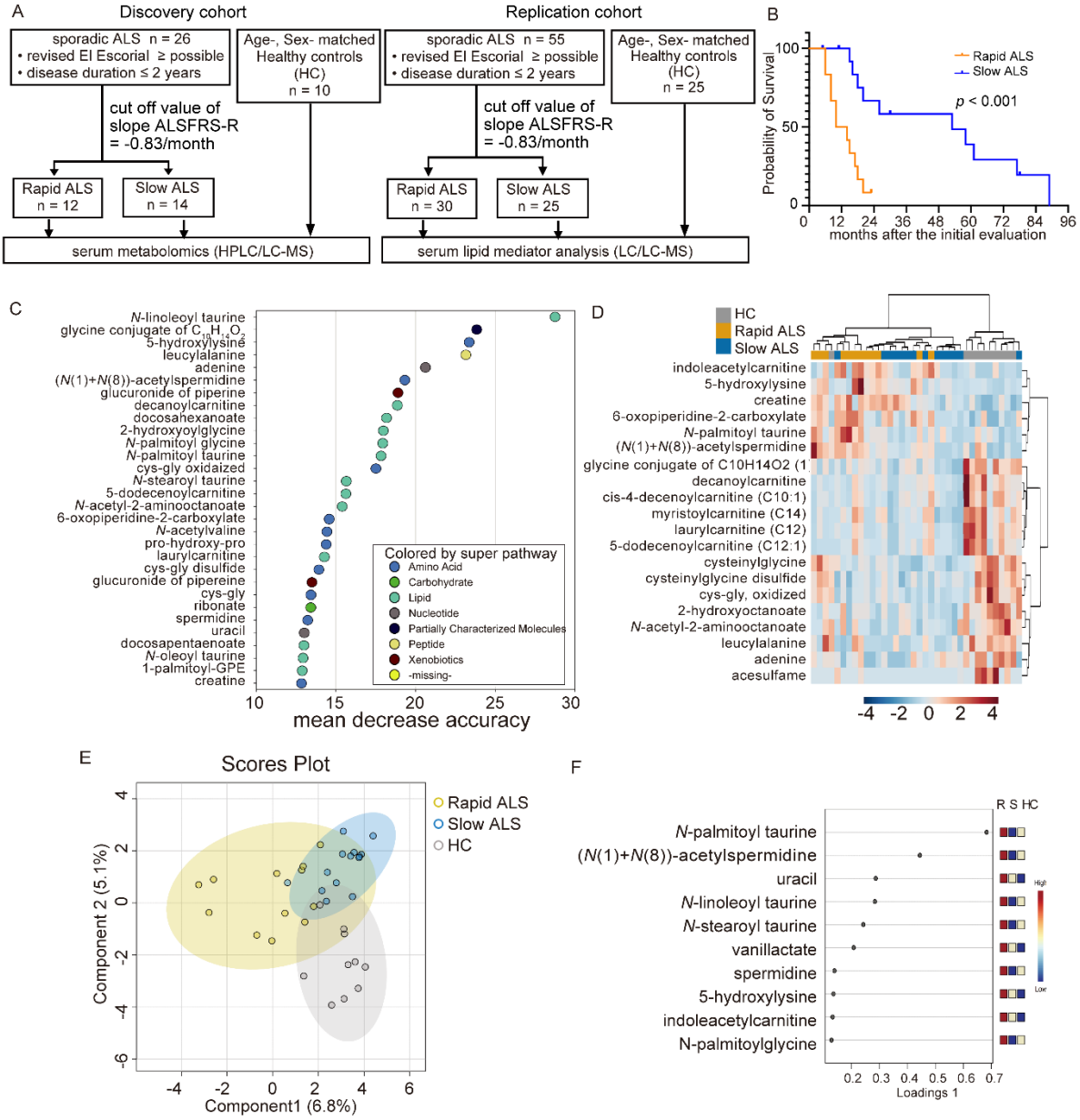

(**A**) Flow chart of metabolome analysis. For discovery cohort, we included subjects with definite, probable, or possible ALS that met the revised El Escorial criteria and had disease duration less than 2 years. Subjects with ALS were divided into rapidly progressive (Rapid ALS, n = 12) and slowly progressive (Slow ALS, n = 14) groups according to the median longitudinal change in ALSFRS-R (slope ALSFRS-R) from the first evaluation to 6 months. Rapid ALS was defined as a decline of ≥5 points in ALSFRS-R over 6 months (slope ALSFRS-R ≤ −0.83/month), and the others were classified as Slow ALS. Ten age- and sex-matched healthy controls were also

included. In the replication cohort, 55 ALS patients and 25 healthy controls were included. ALS patients were similarly classified using the same cut-off value (Rapid ALS, n = 30; Slow ALS, n = 25). (**B**) Kaplan-Meier curves of Rapid ALS and Slow ALS groups (median survival: 12 months vs. 53 months, p = 0.0004, log-rank test). The primary endpoint was defined as the introduction of tracheostomy positive pressure ventilation (TPPV) or death of the patient. (**C**) Top 30 metabolites that discriminate among Rapid ALS, Slow ALS, and healthy controls by random forest classification. The metabolites were ranked according to their mean decrease accuracy. (**D**) Heatmap analysis of the top 20 metabolites identified by one-way ANOVA. (**E**) Sparse partial least squares discriminant analysis (sPLS-DA) plots by MetaboAnalyst 6.0 to discriminate Rapid ALS, Slow ALS, and healthy controls (HC). (**F**) Loading plots of the top 10 metabolites by sPLS-DA shown in (E).

Figure 2. Alteration in *N*-acyl taurine metabolism among patients with rapidly progressive ALS, patients with slowly progressive ALS, and healthy individuals and their correlation with disease progression in the discovery cohort and the replication cohort

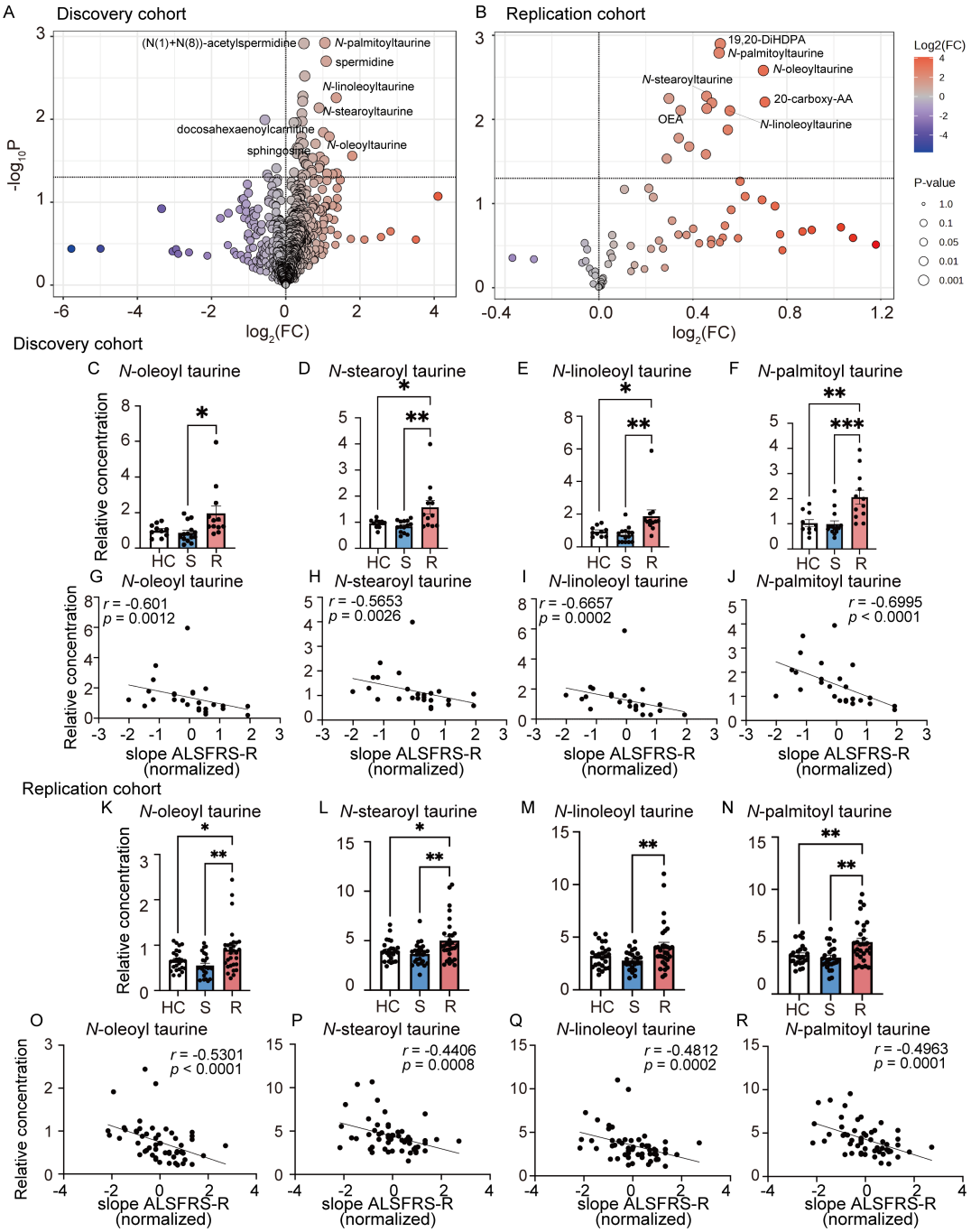

(**A**) Volcano plot of serum metabolomics analysis comparing between Rapid ALS patients and Slow ALS patients in the discovery cohort. (**B**) Volcano plot of serum lipid mediator analysis comparing between Rapid ALS patients and Slow ALS patients in the replication cohort. (**C–F**) Serum levels of *N*-acyl taurine metabolism in the discovery cohort (C, *N*-oleoyl taurine; D, *N*-stearoyl taurine; E, *N*-linoleoyl

taurine; F, *N*-palmitoyl taurine). (**G–J**) Correlation between the serum levels of N-acyl taurines and the prospective, longitudinal change in ALSFRS-R between the first and second evaluations (slope ALSFRS-R) in the discovery cohort (G, *N*-oleoyl taurine; H, *N*-stearoyl taurine; I, *N*-linoleoyl taurine; J, *N*-palmitoyl taurine). (**K–N**) Serum levels of *N*-acyl taurine metabolism in the replication cohort (K, *N*-oleoyl taurine; L, *N*-stearoyl taurine; M, *N*-linoleoyl taurine; N, *N*-palmitoyl taurine). (**O–R**) Correlation between the serum levels of N-acyl taurines and slope ALSFRS-R in the replication cohort (O, *N*-oleoyl taurine; P, *N*-stearoyl taurine; Q, *N*-linoleoyl taurine; R, *N*-palmitoyl taurine). The discovery cohort was analyzed by broad untargeted metabolomics, whereas the replication cohort was analyzed using a targeted lipid mediator panel; therefore, the total number of detected analytes differed between the two cohorts. ALSFRS-R slope values were transformed using the Yeo–Johnson transformation before correlation analysis. One-way ANOVA and Tukey's post hoc analysis were performed (*$p < 0.05$, **$p < 0.01$ and ***$p < 0.001$). HC, healthy controls; R, Rapid ALS; S, Slow ALS. A coefficient value (r) of 0.40–0.59 is considered moderate, while 0.60–0.79 is considered strong in Spearman's rank correlation coefficient. Error bars indicate the SEM.

Figure 3. Kaplan–Meier survival curves based on serum *N*-acyl taurine levels in the discovery and replication cohorts.

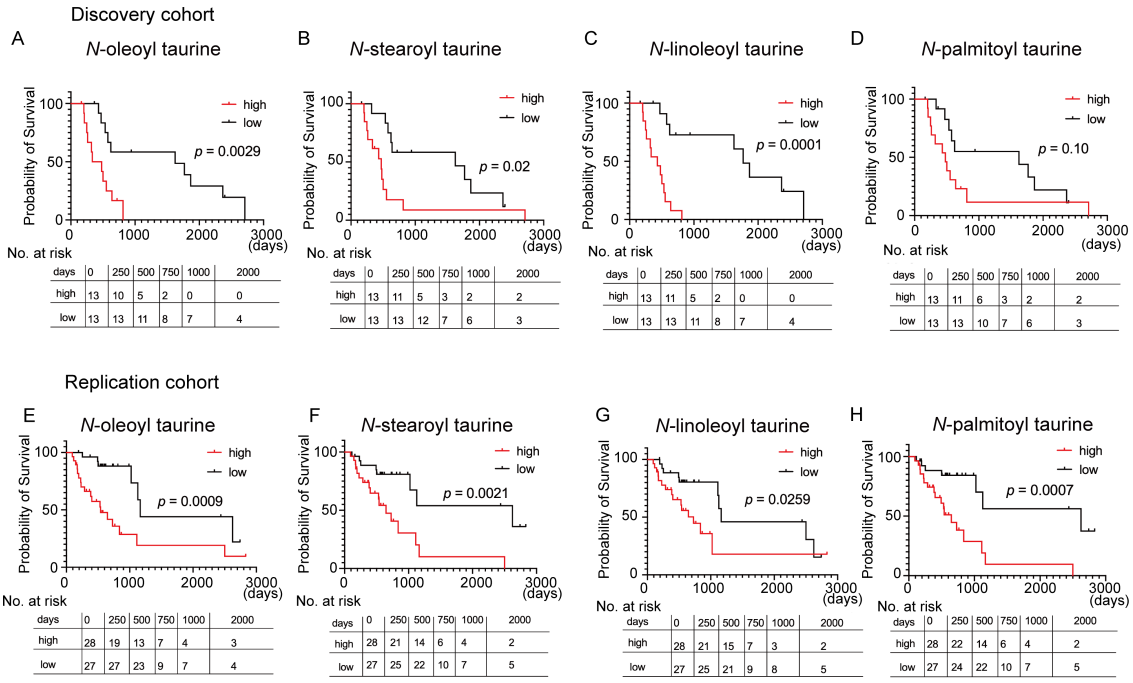

(**A–D**) Kaplan–Meier survival curves of the discovery cohort stratified by serum levels of *N*-acyl taurines: (A) *N*-oleoyl taurine, (B) *N*-stearoyl taurine, (C) *N*-linoleoyl taurine, and (D) *N*-palmitoyl taurine. (**E–H**) Kaplan–Meier survival curves of the replication cohort for the corresponding metabolites: (E) *N*-oleoyl taurine, (F) *N*-stearoyl taurine, (G) *N*-linoleoyl taurine, and (H) *N*-palmitoyl taurine. In both cohorts, patients were divided into high and low groups based on the median serum concentration of each *N*-acyl taurine. The primary endpoint was defined as the introduction of tracheostomy positive pressure ventilation (TPPV) or death of the patient. Log-rank test was used to compare survival between groups.

Figure 4. Cellular assays of compounds targeting the expanded endocannabinoid system and efficacy of PF-04457845 in NSC-34 cells and iPSC-derived motor neurons from sporadic ALS patients

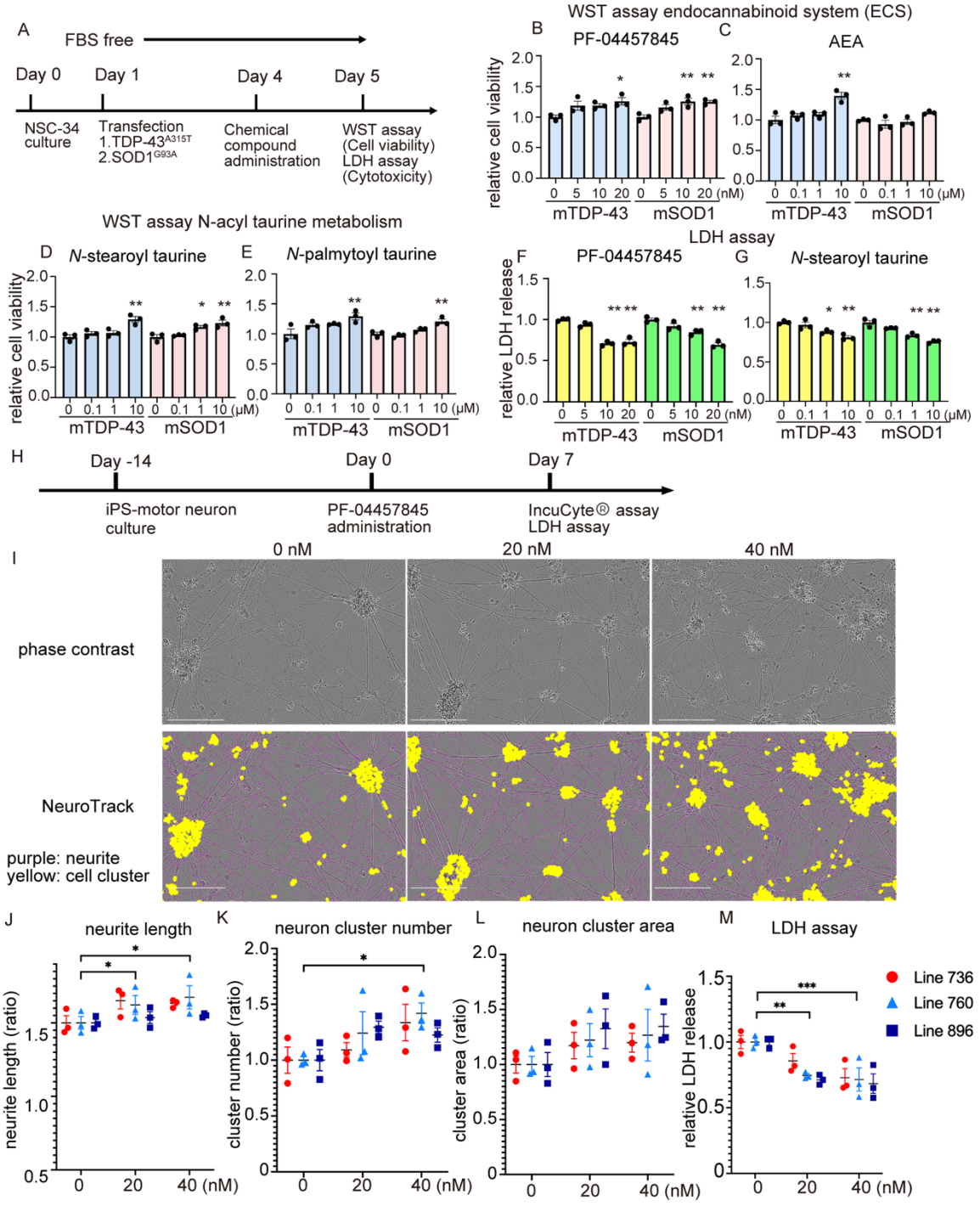

We tested a total of 29 compounds that target the identified metabolic pathways. We used NSC-34 cells transiently overexpressing TDP-43^{A315T} or SOD1^{G93A} and assessed cell viability using the WST-8 assay and cytotoxicity using the lactate dehydrogenase (LDH) assay. Results for the representative agents which modulate the expanded endocannabinoid system including *N*-acyl taurines are shown in this figure, and the other results are summarized in Supplemental Table S6. (**A**) Protocol of the cell

viability assay. (**B–E**) Effects of compounds targeting expanded endocannabinoid system (B, PF-04457845; C, arachidonoyl ethanolamide [AEA]), and *N*-acyl taurine in expanded endocannabinoid system (D, *N*-stearoyl taurine; E, *N*-palmitoyl taurine), on cell viability. Neuroprotective effects of PF-04457845 and *N*-stearoyl taurine were examined by LDH assays (**F**, PF-04457845; **G**, *N*-stearoyl taurine). (**H**) Protocol of administration of PF-04457845 on iPSC-derived motor neurons (iPS-MN) derived from three sporadic ALS patients. (**I**) Analysis of cell morphology by IncuCyte SX5®. iPS-MN were captured by phase separation and neurites (purple) and cell clusters (yellow) were automatically recognized by NeuroTrack algorithm. (**J**) The result of neurite length (N=3 each from three iPS-MN). (**K**) The result of number of cell clusters (N=3 each from three iPS-MN). (**L**) The result of area of cell clusters (N=3 each from three iPS-MN). (**M**) The result of LDH assay (N=3 each from three iPS-MN).

For NSC-34 cells, one-way ANOVA followed by Dunnett's multiple-comparisons test was performed, with each concentration compared with the baseline condition. For iPSC-derived motor neurons, data were analyzed using a mixed-effects model, with treatment as a fixed effect and iPSC line as a random effect, followed by Dunnett's multiple-comparisons test. (*$p < 0.05$, **$p < 0.01$, ****$p < 0.0001$). Scale bars, 200 μm. Error bars indicate the SEM.

Figure 5. In vivo analysis of hit compounds in SOD1^{G93A} transgenic mice

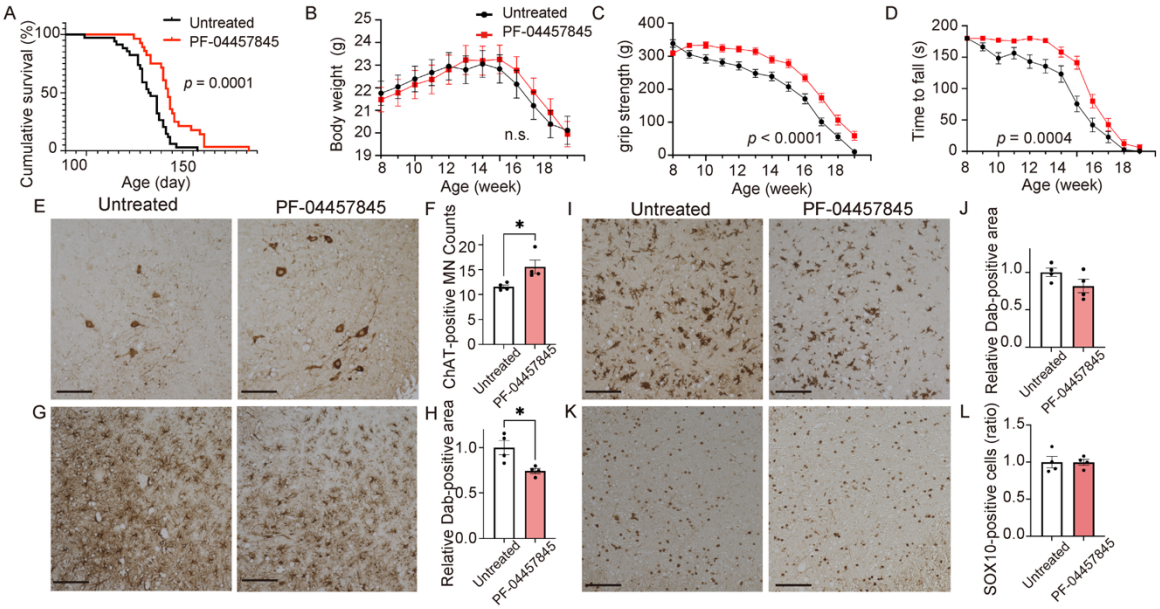

(**A**) Survival of SOD1^{G93A} transgenic mice treated with PF-04457845 (~1 mg/kg/day, PF-04457845), or unmodified chow (Untreated) (n = 28, 34; median survival, 138, 129.5 days, respectively; $p = 0.0001$, log-rank test). PF-04457845 extended the survival of SOD1^{G93A} transgenic mice compared with untreated mice. (**B**) Body weight, (**C**) grip strength and (**D**) rotarod test in SOD1^{G93A} transgenic mice treated with PF-04457845 or unmodified chow. Body weight was not significantly different, whereas grip strength ($p < 0.0001$) and rotarod test ($p = 0.0004$) were significantly improved by PF-04457845 (two-way ANOVA). To impute values after the endpoint, the final body weights were carried forward and the values of grip strength and rotarod were imputed to zero. (**E–L)** Immunohistochemistry images and quantitative analysis of immunoreactivity for choline acetyltransferase (ChAT) (E, F), glial fibrillary acidic protein (GFAP) (G, H), ionized calcium-binding adapter molecule 1 (IBA-1) (I, J), and Sry-related HMG-BOX gene 10 (SOX10) (K, L) in the ventral horn of the spinal cords of 16-week-old mice treated with PF-04457845 (n = 4) or unmodified chow (n = 4). Scale bars: 100 μm, Error bars indicate the SEM. Survival was analyzed using the Kaplan–Meier method and compared by the log-rank test. Body weight and motor functions were analyzed by two-way ANOVA, and p values for the treatment effect are shown in the figure. Quantified pathology measures were compared using two-sided unpaired t-tests. *$p < 0.05$.

Figure 6. Lipidomics analysis of spinal cords of wild-type and SOD1^{G93A} transgenic mice with or without treatment with PF-04457845

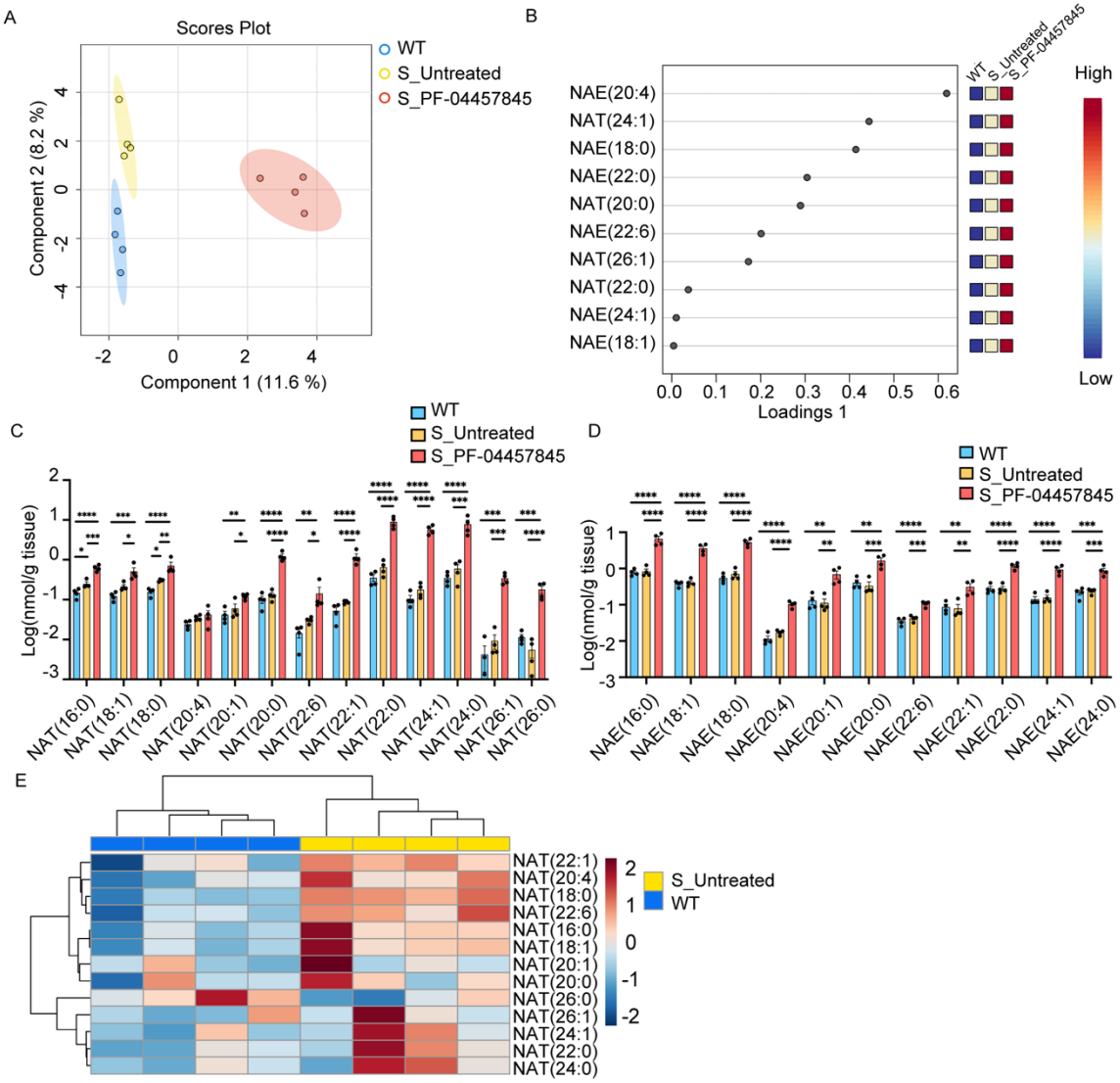

(**A**) Sparse partial least squares discriminant analysis (sPLS-DA) plots by MetaboAnalyst 6.0 to discriminate wild-type mice (WT, n = 4), untreated SOD1^{G93A} transgenic mice (S_Untreated, n = 4) and SOD1^{G93A} transgenic mice treated with PF-04457845 (S_PF-04457845, n = 4). Loading plots of the top 10 lipids by sPLS-DA are shown in (**B**). (**C**) Log transformed concentrations of *N*-acyl taurines (NAT). (**D**) Log transformed concentrations of *N*-acyl ethanolamine (NAE). (**E**) Heatmap analysis of *N*-acyl taurines comparing untreated SOD1^{G93A} transgenic mice and wild-type mice. Error bars indicate the SEM. *$p < 0.05$, **$p < 0.01$ and ***$p < 0.001$, ****$p < 0.0001$. One-way ANOVA and Tukey's post hoc analysis were performed.

Figure 7. RNA-Seq analysis of the spinal cords from SOD1^{G93A} transgenic mice treated with PF-04457845

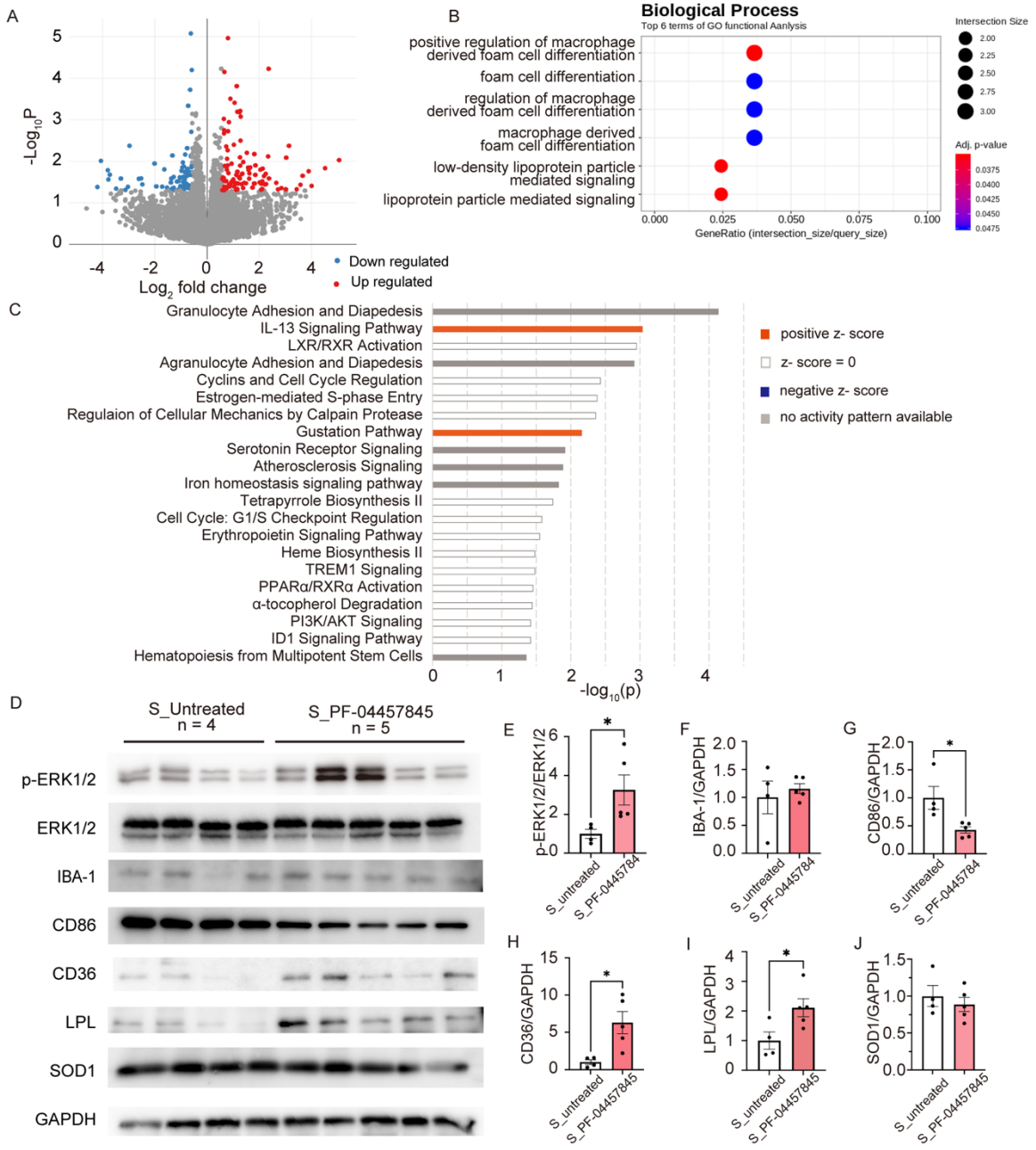

(**A**) Volcano plot of the differentially expressed genes of the bulk spinal cords between the mice treated with PF-04457845 (n = 4) and the untreated mice (n = 4). (**B–C**) Gene Ontology enrichment analysis for up-regulated genes (B) and Ingenuity Pathway Analysis (IPA) (C) analysis of genes with significant expression changes (fold change < -1.5 or > 1.5, $p < 0.05$) in the spinal cords of 16-week-old SOD1^{G93A} transgenic mice treated with PF-04457845 (n = 4) compared with untreated mice (n = 4). (**D**) Western blot analysis of proteins downstream of cannabinoid receptor type 2

(CB2), microglial markers, and superoxide dismutase 1 (SOD1) in the spinal cords of 16-week-old $SOD1^{G93A}$ transgenic mice treated with PF-04457845 (S_PF-04457845, n = 5) and untreated $SOD1^{G93A}$ transgenic mice (S_untreated, n = 4). (**E–J**) Quantitative analysis of phosphorylated ERK/ERK (E), ionized calcium-binding adapter molecule 1 (IBA-1) (F), CD86 (G), CD36 (H), lipoprotein lipase (LPL) (I), and SOD1 (J). The levels of IBA-1, CD86, CD36, LPL, and SOD1 were normalized to GAPDH levels. Error bars indicate the SEM. *$p < 0.05$, unpaired two-sided *t* test.

Figure 8. Single-nucleus RNA-Seq analysis of the spinal cords from SOD1^{G93A} transgenic mice treated with PF-04457845

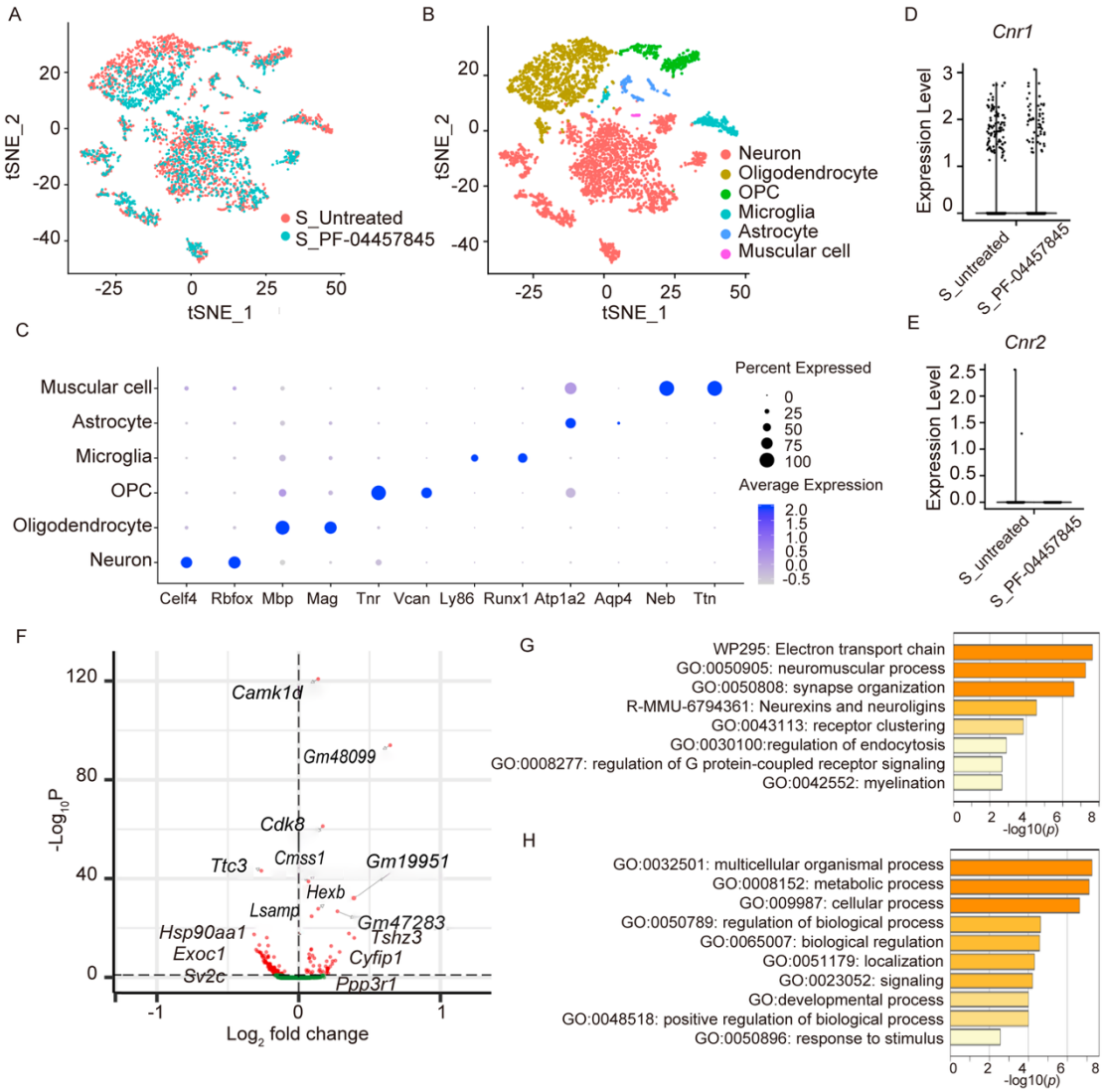

We performed single-nucleus RNA sequencing on the spinal cords of 16-week-old SOD1^{G93A} transgenic mice treated with PF-04457845 (S_PF-04457845) or unmodified chow (S_Untreated). (**A**) t-Distributed stochastic neighbor embedding (t-SNE) plot color-coded by sample, with red for untreated mice and blue for PF-04457845-treated mice. (**B**) t-SNE plots of all cells sequenced showing six cell types. (**C**) Dot plot depicting the expression of specific markers for each cell type. (**D–E**) Expression levels of CB1 (D) and CB2 (E) in the neuron cluster of each sample. (**F**) Volcano plot of the differentially expressed genes in the neuron cluster from the mice treated with PF-04457845 compared to that from the untreated mice. (**G–H**) Gene Ontology enrichment analysis for upregulated (G) and downregulated (H) genes between the neuron clusters from the mice treated with PF-04457845 and the untreated mice